Femtosecond Laser Mass Spectroscopy of Cyclic Aromatic Hydrocarbons

By

Amit Bagga

December 2017

Thesis submitted to the Faculty
of Graduate Studies in partial fulfillment of
the requirements for a Master's degree in Physics

Department of Physics Faculty of
Science University of Ottawa

Contents

Table of Figures

Table of Abbreviations

ADK: Ionization rate function developed by Ammosov, Delone and Krainov

ASE: Aromatic Stabilization Energy

BBO: Beta-Barium Borate crystal

HWP: Half Wave Plate

HHG: High-order harmonic generation

HOMA: Harmonic Oscillator Model of Aromaticity

MCP: Micro-channel plate

MO-ADK: Particularized ADK model for molecules

MPI: Multi-Photon Ionization

NICS: Nucleus Independent Chemical Shift

NSDI: Non-Sequential Double Ionization

SAE: Single Active Electron Approximation

SFA: Strong Feld Approximation

SFI: Strong Field Ionization

QWP: Quarter Wave Plate

XUV: Extreme Ultra-Violet radiation

Abstract

Cyclic Aromatic molecules are the subject of continued research due to their highly advantageous characteristics which can be exploited in the areas of pharmaceuticals, material science and nano-electronics. While the defining properties and criteria for a molecule to be considered aromatic are very specific and well established, the degree of aromaticity of these molecules and their corresponding ordering remains a source of continued debate. Given that the macroscopic aromatic properties are fundamentally rooted in the underlying electronic structure and molecular dynamics, these properties can be probed in numerous ways. One such method is to exploit the strong laser field as it pertains to non-linear light-matter interaction. More specifically, the study of photoionization, as a direct resultant effect of strong field light-matter interaction, gives us direct insight into electronic and spatial properties as captured via mass spectroscopy. As a strong-field process, photoionization is effective because the variables that influence its results are also the ones that define aromaticity thus a correlation can be postulated. Other strong field advanced techniques to probe aromacity such as High Harmonic Generation (HHG) have already been successful shown by our group to be effective spectroscopic tools. In this way, photoionization provides supporting evidence to enhance the understanding of these novel spectroscopic tools. This thesis demonstrates that photoionization mass spectroscopy can be used as a probe into the aromaticity order of 5-membered cyclic aromatic molecules. Furthermore, the thesis will show that photoionization results correlate with the previously conducted HHG studies in this area thus further supporting these techniques as sensitive spectroscopic tools into aromaticity. The first part of this thesis describes the characterization of aromatic molecules and the corresponding process to obtain photoionization results that can be correlated to aromaticity. In the second part, these results are compared to the theoretical model and HHG demonstrating consistent results. The third and final component of this thesis describes future work, namely two-colour control of photoionization which is intended to provide greater resolution and variation of photoionization spectra thereby providing a more comprehensive and conclusive understanding of the proposed correlation with aromaticity.

Chapter 1: Background

1.1 Overview

Cyclic Aromatic Hydrocarbon molecules, which are fully described in Chapter 2, have vitally important applications in many diverse facets of contemporary industry and technology. Their macroscopic chemical and physical properties are unique to other cyclic structures with similar composition thus greater understanding of their makeup continues to be a focus of current research permitting greater exploitation of their beneficial properties. As will be discussed in Section 1.5, the problem with the current understanding of 5-membered aromatic molecules is the lack of a cohesive approach to quantifying their aromaticity. Aromaticity is used to describe molecules that are cyclic, planar and have resonance bonds resulting in a special stability in comparison to other non-aromatic molecules with similar geometry. Contemporary work in the field has approached aromaticity from the modelling and computational perspectives, using for example, axioms such as bond lengths, magnetic susceptibility and stabilization energy to form the basis of measuring aromaticity. While these approaches are diverse and provide qualitative ordering, they lack conclusive correlation to the criteria that actually make these cyclic structures aromatic to begin with, that is, their electronic structures and dynamics. To advance our understanding of these structures, one of the principal tools we have at our disposition is the interaction of light with matter. The advent of femtosecond lasers has enabled the study of molecular interactions in the strong field regime with attosecond resolution capable of probing dynamics at atomic timescales. The outcome of these atomic scale interactions can be effectively gauged via spectroscopy which can be applied to the various stages and processes described by strong field laser physics. Photoionization of molecules is one such process which under the variable conditions of intensity, polarization and wavelength can provide us key insights into the construct of aromatic molecules. Recent work by our group has also demonstrated advances in the use of High Harmonic Generation (HHG) yield as an effective spectroscopic tool in conclusively quantifying the order of molecular aromaticity. These recent advances are introduced in Section 1.6 and are compared to our results on photoionization of aromatic molecules in Section 5.5 of this thesis.

1.2 Motivation for the Experiment

Recently, HHG spectroscopy was used to quantify aromaticity. The motivation for this study is to develop a conclusive basis for quantifying aromaticity by investigating photoionization, which is the first of 3 steps in the HHG process. HHG also includes the steps of electron propagation and recombination. The ability to precisely control photoionization via the accurate application of laser intensity and polarization variation permit detailed studies of the unique properties exhibited by aromatic molecules. For example, the variation of polarization can provide valuable insight into the electronic structure of aromatics via the analysis of the transverse spreading of the electron wave-function after tunnelling. This is described in detail in Section 5.3. Furthermore, since the results of the HHG yield studies discussed in the previous Section involve the combination of electronic and temporal dynamics from three unique steps, it is advantageous to break these steps down and analyze the contribution of each to the overall process. The specific result of electronic and temporal effects from photoionization is described in Section 5.4. Via this analysis, the distinct contribution of photoionization will ultimately permit greater understanding of the correlation between the resultant spectra and our understanding of the structural dynamics of cyclic aromatic molecules.

1.3 Light – Matter Interaction

The study of nonlinear light – matter interaction is possible as a result of the strong laser field produced by ultra-short and highly intense pulses on the order of 10^{14} W/cm^2. Nonlinear interaction arises from the fact that the photon energy is significantly less (~ 1.5 eV) than the ionization potential of the molecule (typically 8-12 eV). The laser field is comparable in strength to the molecular binding field thereby altering the electronic properties of the molecule itself. In contrast to high intensity, ionization under lower intensity laser fields can only occur if the energy of the absorbed photon is higher than the ionization potential of the electron. Therefore, application of the strong field laser directed upon the aromatic molecules of interest will generate ionization of singly and multiply charged ions in only a few optical cycles. As will be shown in chapter 3, the ions can then be channelled via a Time-of-Flight (TOF) for spectroscopic analysis.

Strong field ionization of molecules occurs via two distinct regimes, namely Multi-Photon Ionization (MPI) and Tunnelling which are defined in Section 1.4. As these processes are quantum mechanical in nature, both will be present to some degree during photoionization and will vary in importance depending on the E-field variables and the phenomena being studied. The application of these two areas to the experiment and the effects of variation in intensity, polarization and wavelength are described in Chapter 4.

1.4 Strong Field Laser Interaction with Molecules

When compared with atoms, molecules are significantly more complex. The interaction of the laser strong field with molecules has many influencing variables that when altered result in changes to the electronic structure and dynamics. Therefore these variables need to be carefully controlled and observations analyzed and compared to atoms and other molecules, both aromatic and non-aromatic, to understand how they are impacted by light-matter interaction. The key observables from the strong field interaction with the aromatic molecules include, for example, their saturation intensities, ionization yields, ellipticity dependence and fragmentation. These are described in detail in Chapter 5. To understand how the variables interplay with the molecule's potential barrier and corresponding electron wave-function to produce the observed effects, it is important to first define the E-field and then define the regimes under which the E-field interaction will provide different responses. This description is addressed in Sections 1.4.1 through 1.5.2.

1.4.1 Ionization Regimes

As introduced earlier, the focus of strong field experimentation with the aromatic molecules for this thesis is photoionization. As delineated in Section 1.3, within this area of interest there are two regimes, namely Multi-Photon Ionization (MPI) and Tunnelling. Before describing these regimes however, it is important to make reference to the E-field variables that will describe the transition between these regimes. The E-field of a laser is fundamental to the understanding of light-matter interaction and is described as follows for few-cycle pulses [1]:

$$\boldsymbol{E(t) = E_0 \sin(\omega t + \varphi)} \quad \textbf{(1.1)}$$

Where E_0 is the envelope of the field, ω is the carrier frequency and φ is the carrier-envelope phase. The equation is of importance because the pulse energy, wavelength and phase all have significant roles in the outcome of the light-matter interaction. In the strong laser field, the E-field applied per unit area needs is to be sufficient enough to absorb photons. Direct photon absorption is possible via a high intensity and continuous rate laser thereby producing an E-field intense enough to alter the binding energy of the molecule. The important relationship between the E-field and intensity is as follows [1]:

$$\boldsymbol{E = \left[\frac{2I}{\varepsilon_0 c}\right]^{\frac{1}{2}}} \quad \textbf{(1.2)}$$

where $\mathcal{E}_0$ is the permittivity of free space, c is the speed of light and I is the intensity. The interaction of strong field radiation with molecules results in significant energy absorption by the molecule. While ionization is the primary channel of energy release following absorption, fragmentation of the molecule is also a possible mechanism that provides valuable insight on the stability of aromatic molecules and is described in Section 5.8. Sections 1.4.2 through 1.5.2 describe the mechanism of strong field ionization, specifically the promotion of the electron into the continuum via specific mechanisms.

1.4.2 Multi-photon Ionization (MPI)

MPI results from an electron gaining enough energy to become ionized by absorbing numerous photons continuously. It is based on the deposition and absorption of *N* high intensity laser photons onto the molecule in a time period defined by position-time uncertainty principle permitting the electron to be ionized in a step-like process independent of molecular energy levels. The number of photons needed to be deposited for the process of multi-photon ionization to occur under the influence of the strong field is [1]:

$$\boldsymbol{N\hbar\omega \geq E_I \geq (N-1)\hbar\omega} \quad \textbf{(1.3)}$$

where E_I is the binding energy of the electron. This describes that the number of photons required depends on the photon energy such that their product is greater than the binding energy. MPI is the predominant process observed at the 800nm wavelength and increases proportionally with intensity given the distorting effect that high intensity has upon the potential barrier. Of note, at longer wavelengths, tunnelling becomes more pronounced as described in Section 1.4.3. As the number of photons absorbed by the molecule increases, the probability of MPI becomes smaller as based on the following relationship [12]:

$$\boldsymbol{\rho(n) = \sigma_n I^n} \quad \textbf{(1.4)}$$

Where ρ is the probability of absorbing n photons and σ_n is the cross sectional area of ionization and I is the intensity. For example, ionization of the Xe atom (I_p=12.3) is an 8^{th} order non-linear process since the typical photon energy is 1.55 eV (at 800nm).

1.4.3 Tunnelling

Tunnelling is a phenomenon described via the electron wave-function where there is a non-vanishing probability for the electron to transition to the continuum. Under the right E-field conditions, the quantum tunnelling regime will occur with higher probability as based on laser frequency and tunnelling time. Firstly, a temporary deformation of the Coulomb potential well is caused by the laser field. Ionization then results if the laser E-Field is comparable in strength to the coulomb potential and is of a low enough frequency that the electron subjected to that field has sufficient time to transit across the molecule's potential barrier.

The Coulomb potential barrier (V) as a function of distance (r) from the core with respect to the E-Field (E) is described as:

$$\boldsymbol{V(r) = -kq^2/r + Er} \quad \textbf{(1.5)}$$

A classical method to estimate the intensity required for tunnelling is based on the "Over-the-Barrier" threshold (I_{th}) described as follows [1]:

$$\boldsymbol{I_{th} = KI_P^4 / (16Z^2)} \quad \textbf{(1.6)}$$

Where I_p is the ionization potential and Z is the charge state of the ion. K is a constant and equals 1 when expressed in atomic units (or 6.4 x 10^{10} when I_p is expressed in eV) and I_{th} is in W/cm^2. Using the above expression for a singly charged state and corresponding ionization potentials of 8-20 eV, the threshold intensity (as it relates to the experiment) results in a minimum intensity of 2 x 10^{13} W/cm^2 which is consider valid experimentally. Theoretically, the factor which differentiates the two regimes is the Keldysh parameter which is explained in greater detail in Section 1.4.4.

1.4.4 Keldysh Parameter

While the I_{th} expression provides a rough approximation of when tunnelling will occur, to obtain a more accurate prediction, the quantum mechanical nature of the process must be taken into account via the Keldysh parameter. The Keldysh parameter (γ) describes the likelihood of ionization via the MPI or tunnelling regimes as per the following expression [2]:

$$\boldsymbol{\gamma = (I_p/2U_p)^{1/2}} \quad \textbf{(1.7)}$$

Where U_p is the ponderomotive energy and is described as [2]:

$$U_P = {e^2E^2}/{4m\omega^2} \quad \textbf{(1.8)}$$

Where *e*, *m* and ω are the charge, mass and angular frequency respectively and *E* is the electric field strength. Ponderomotive energy describes the oscillation energy that a free electron will have in the E-field of the laser pulse.

A Keldysh parameter of less than 1 (γ<1), describes a depressed coulomb barrier and therefore identifies the tunnelling regime. A Keldysh parameter of more than 1 (γ>1) describes absorption of multiple photons permitting the electron to ionize directly. A Keldysh parameter of greater than 1 does not necessarily imply that there is no contribution from the tunnelling regime however the probability is significantly reduced. Therefore γ<<1 describes a predominant tunnelling regime and γ>>1 describes a predominant multi-photon regime [1]. The two regimes are illustrated pictorially in the Figure 1 showing MPI on the LHS and tunnelling on the RHS:

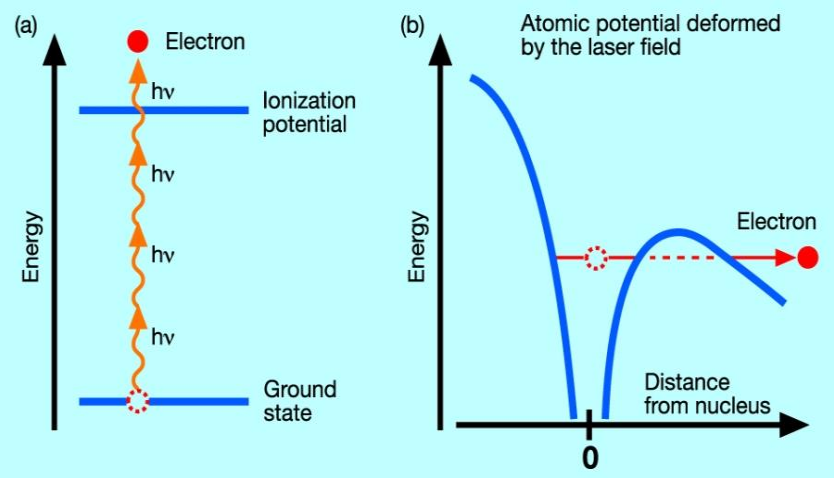

Figure 1: Effect of Variations in the Keldysh Parameter. Shows the different regimes when the parameter is either greater than 1 or less than 1.

Despite its general success at predicting ionization regimes, there are limitations to the use of the Keldysh parameter. In particular, it is based only on the ionization potential and laser frequency

therefore its use as a predictor for the overall interaction of the laser field with complex molecules is limited. Therefore, it is to be used as an approximation only for the contribution of ionization from the two regimes.

1.5 Multiply Charged Ions

In the previous section, the ionization regimes are described for promoting an electron to the continuum, firstly via MPI and secondly via tunnelling. Once ionized, under certain E-field variables of intensity, polarization and optical phase, the molecule can undergo further ionization via two mechanisms of sequential and non-sequential ionization. This is described in Sections 1.5.1 and 1.5.2.

1.5.1 Sequential Ionization

In sequential ionization, E-field strengths produced by the laser are sufficiently intense to multiply ionize a singly charged molecule directly. The sequential nature of the ionization processes is depicted in the two molecular equations:

$$\sim h\omega + M \rightarrow M^{+} + e^{-} \qquad \sim h\omega + M^{+} \rightarrow M^{2+} + e^{-}$$

1.5.2 Non-Sequential Double Ionization (NSDI)

In NSDI, the process begins with the molecule having absorbed energy and having ionized an electron as per the description in Section 1.4.1 in either regime. The freed electron propagating in the continuum will then move under the influence of the laser field, gaining energy in the process by a factor of $3.17U_p$, where U_p is the ponderomotive energy described in Section 4.4. Depending on the laser field polarization, the electron can potentially have a re-collision with the parent ion core resulting in one of three outcomes, either it scatters, recollides with another electron or recombines with the parent ion. As illustrated in Figure 2, for NSDI to occur, the

propagating electron recollides with the parent ion resulting in the ejection of a secondary electron thereby doubly ionizing the parent molecule:

$$\sim h\omega + M \rightarrow M^{+} + e^{-} \rightarrow M^{2+}$$

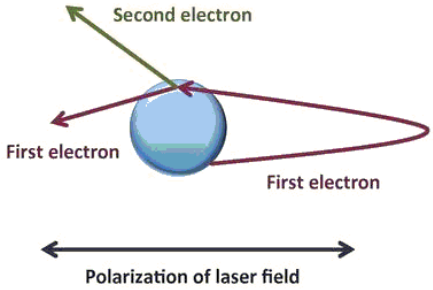

Figure 2: Non-Sequential Double Ionization as the result of a recolliding electron with the Parent Ion

The electron trajectories can be controlled by laser polarization thereby influencing the probability of recollision and hence NSDI. Therefore laser polarization is an effective method at distinguishing between SI and NSI. For example, in linear polarization, both processes can be active however in circular polarization NSDI disappears given that the electron is driven away from the parent ion core. The physics surrounding this is explained in Section 5.3. Notwithstanding this differentiation technique, it was noted that the presence of doubly charged molecules in the experiment was the result of both SI and NSDI acting together. Therefore, these two processes were fundamental to interpreting the photoionization results given their relative contribution on the overall yield. As will be shown in Chapter 5, the contribution from both mechanisms can be discriminated based on the relative slopes of doubly charged ions as a function of singly charged ions.

1.6 High Harmonic Generation Three Step Model

The HHG involves 3 distinct steps: Firstly, electron photoionization via MPI or tunnelling, secondly electron propagation in the continuum and lastly recombination. In acknowledging the complexity of the 3 steps and their independent variables, it becomes critically important to

properly distinguish and define the photoionization phase within the overall sequence of the HHG model. A pictorial view of these steps is presented in Figure 3:

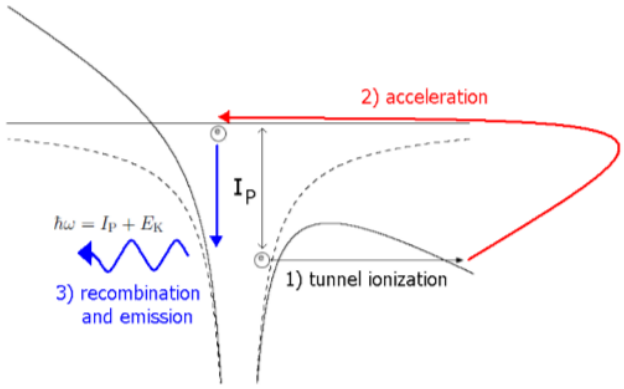

Figure 3: HHG 3-Step Model showing the tunnel ionization, Propagation in the laser field (acceleration) and Recombination

Specifically, photoionization of the electron from the parent molecule results from the distortion of the molecule's atomic potential by the laser field followed by the electron tunnelling into the continuum. Second, the electron will accelerate in the continuum under the influence of the laser field, moving outward from the molecule and then returning based on the shift in polarity of the laser E-field. In the third step, the electron recombines with the parent molecule along with the resultant emission of XUV photons. This HHG emission can be characterized based on the spatial and temporal observation characteristics resultant from the molecule's properties and interaction with the high intensity laser. A typical spectrum of HHG involves a 'Perturbative' region followed by a 'Plateau' and a 'Cut-off' as depicted in Figure 4 [1]:

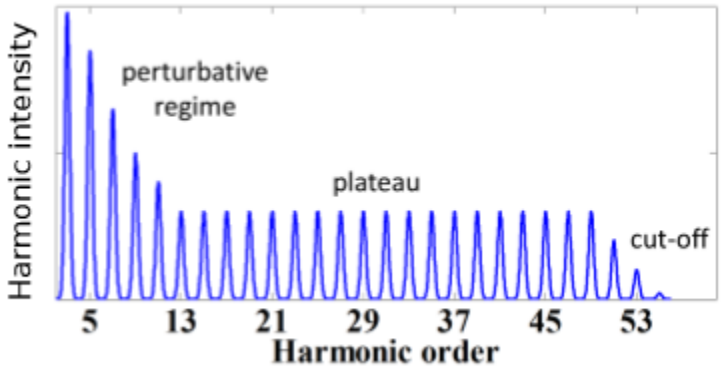

Figure 4: Typical spectrum of High Harmonic Generation showing the 3 regions including the Perturbative, Plateau and Cut-Off.

As introduced earlier, Alharbi et al (2015) have demonstrated the first quantitative investigation of the contribution of π-electrons to the enhancement of HHG in aromatic molecules [3]. In Figure 5, the harmonic yield of Furan, an aromatic molecule, is observed to be significantly higher in comparison to Dihydrofuran, a non-aromatic molecule.

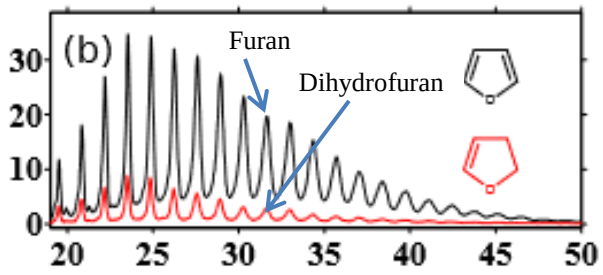

Figure 5: HHG Spectra of Furan (black) in comparison to Dihydrofuran (red) shows enhancement of HHG in aromatic molecules

Given the enhancement shown in HHG for aromatic molecules and the importance of understanding the contributions from the 3-steps, the motivation for this thesis was specifically to perform a comparison of spectra resultant uniquely from photoionization. This is aimed to provide insight into the overall 3 step model, thus delineating observed effects from the propagation and recombination stages.

Chapter 2: Cyclic Aromatic Hydrocarbon Molecules

Chapter 1 was focused on nonlinear light – matter interaction and the different strong field regimes that arise from the interaction with molecules. Chapter 2 centres on the specific aromatic molecules under study.

Aromatic molecules are cyclic structures in which each ring atom is a participant in a π-orbital resulting in π electron delocalization. To be considered an aromatic molecule, there are very specific conditions required. Firstly, the molecule must be cyclic meaning that the series of atoms bond together to form a ring. Second, the molecule must follows Hückel's rule requiring that there be (4n+2) π-orbital electrons which results in electron de-localization. Third, the molecule must be conjugated which requires that the de-localized electrons in the ring molecule all participate in p-orbitals. Fourth, the molecule must be planar. If any one of these conditions is not met, then the molecule cannot be considered aromatic.

Aromatic molecules are typically more stable than non-aromatic ones. This stability is demonstrated when the molecule is undergoing multiply charged ionization. In stable molecules, the yield of multiply charged yield will be greater and will not fragment as a result of the sharing and uniformity of distribution of π-orbital electrons [39]. For the electrons to be shared in this way, the molecule must be planer such that the p-oribitals can overlap. This can be explained by looking within the cyclic ring of overlapped p-orbitals, each carbon atom may donate one electron and two electrons are donated from the heteroatom to form a delocalized cloud [40].

Aromatic molecules have unique and distinct properties that motivate contemporary studies and applications. Unique properties such as high stability, high resonance energy, low reactivity, non-polarity and immiscibility in water are highly suitable for diverse applications such as in nano-electronics, material science and pharmaceuticals. In biochemistry for example, aromatic molecules form part of DNA strands and hence their complex interaction with other organic compounds contained in DNA is an important are of research.

2.1 Contemporary Studies into Aromatic Molecules

While aromatic molecules have been the subject of numerous contemporary studies in modern times, their classification in terms of degree of aromaticity order remains inconclusive. Examples of investigations that have attempted to define aromaticity are as follows:

1) Nucleus Independent Chemical Shift (NICS) [6][31]: This computational model is used to calculate the amount of magnetic shielding at the centre of the ring molecule which is understood to contribute to aromatic properties. The more magnetic shielding around the center of a molecule, the higher the degree of aromaticity in the molecule.

2) Harmonic Oscillator Model of Aromoaticity (HOMA) [7]: This is the sum of deviations of the various bond lengths in the ring molecule. Since the bond lengths are stipulated to have an ideal value, these deviations from the ideal define the relative aromaticity order. A bond length of value 1 is considered the ideal therefore deviations away from this value indicate lesser aromaticity order.

3) Ring-current Diamagnetic Susceptibility [8]: When subjected to magnetic fields, molecules can have a current induced in them as based on their magnetic susceptibility. Therefore this measures the degree that a molecule will be susceptible to magnetic field as based on group additivity tables and measured values. The difference between measured and calculated values provides insight into the degree of aromaticity.

4) Aromatic Stabilization Energy (ASE) [9]: This is a measure of π electron stability as based on reaction energy of homodesmotic processes. Homodesmotic processes are reactions in which the constituents form products that have equal numbers of carbon atoms in the same state of hybridization.

The problem with each of these various methods is that they present a different order of aromaticity as depicted in Figure 6. Therefore the photoionization studies conducted in this thesis project will provide supporting evidence in quantifying aromaticity order:

Aromatic Molecule	HOMA	HOMA Rank	ASE	ASE Rank	NICS(1)	NICS Rank	χ_G	χ_G Rank
Benzene	1.0	1	22.5	1	-11.2	1	0.52	1
Pyrrole	0.86	2	20.6	3	-10.5	3	0.41	3
Cyclopentadienide	0.74	3	22.0	2	-10.25	4	0.51	2
Thiophene	0.73	4	18.6	4	-10.7	2	0.34	4
Furan	0.20	5	14.8	5	-9.36	5	0.24	5

Figure 6: Aromatic molecule ordering comparison (values and relative ranking)

2.2 Specific Aromatics under Study

Aromatic compounds can be monocyclic or polycyclic. Furan, Thiophene and Pyrrole are examples of polycyclic heteroarenes where at least one carbon atom is replaced by a heteroatom such as Oxygen, Nitrogen or Sulfur. Specifically, the molecule heteroatom for Thiophene is Sulfur (C_4H_4S), in Furan it is Oxygen (C_4H_4O), and in Pyrrole it is Nitrogen and Hydrogen (C_4H_4NH). Dihydrofuran possesses two additional Carbon atoms and Oxygen as its heteroatom (C_6H_4O). Aromatic Hydrocarbon molecules exist in a variety of cyclic member configurations. 5-membered rings are of particular interest given their unique stability characteristics in relation to the more stable 6-membered rings.

The ionization potential characteristics amongst the three molecules under study are shown in Table 1 indicating the proximity of the ionization potential within the three aromatic molecules:

Aromatic Molecule	Ionization Potential (eV)
Pyrrole	8.20
Thiophene	8.86
Furan	8.88

Table 1: Ionization Potentials for Aromatic Molecules of Interest

It is important to choose molecules with similar I_p since photoionization depends strongly on ionization potential. Since the spread in ionization potentials between the three aromatic molecules is not large enough to produce an appreciable difference in ionization yield, then we can refute this variable as a major consequence in the results. Aside from I_p as a discriminating factor, it is equally critical to select cyclic molecules with equal number of members in the ring. 5-membered cyclic molecules for example have far different properties than 6-membered rings therefore it would not be appropriate to draw a comparison between them. Consequently the molecules chosen were all 5-membered cyclic rings.

Chapter 3: Experimental Setup

3.1 Time-Of-Flight (TOF) Mass Spectroscopy

TOF permits the determination of ion spectra via the precise measurement of the time it takes for the molecules under study to travel from extractor to detector. Once precise time is known, the spectra obtained for the aromatic molecules can be calibrated by using the known m/z ratios of H_2, O_2 or N_2 ions which are present under atmospheric pressure in the drift chamber and whose relative abundance is already known. Using the calculated m/z of the ions and fragments of interest and their respective TOF, their relative abundance is determined and used for analysis. Experimentally, the ions' spectra are confirmed via verification of their respective isotope abundance.

3.2 Laser Used for the Experiment:

The molecular ionization experiments were conducted with an 800nm wavelength Ti: Sapphire laser system capable of producing femtosecond pulses. System components of the laser include a Spectra Physics - Tsunami oscillator and a Spectra Physics – Spitfire Pro amplifier. After amplification, the output power of the laser is 2.7 W (average) with pulse duration of 40 fs, generating intensities between 10^{13} to 10^{15} W/cm^2. Short laser pulse durations are critical to permit MPI due to the time-energy uncertainty principle where the probability for absorption is dependent on the number of photons deposited per unit time on to the molecule:

$$\Delta E \cdot \Delta t \geq \hbar \qquad \textbf{(3.1)}$$

Ultra-short, few cycle laser pulses produced from mode-locked lasers will have pulse durations of femtoseconds or less. For pulses of this duration, optical techniques are required for beam characterization as there are no processes shorter than the pulse itself. Techniques such as autocorrelation are used to measure the duration. During the experiment it was important to

regularly verify the pulse duration to ensure that it was maintained as low as possible (generally below 40fs). This is achieved by a simple shot auto-correlator. In terms of photoionization, pulse energy specifically deposited within the spot size and duration of the laser is of particular importance. Pulse energy E_p is the optical power integrated over time whereas peak power P_p is obtained as a result of the energy taken over the laser's specific pulse duration time ($\boldsymbol{\tau_P}$) as measured with the auto-correlator. The expression that describes this is as follows [1]:

$$\boldsymbol{P_P = f_S \frac{E_P}{\tau_P}} \qquad \textbf{(3.2)}$$

where f_S is a numerical factor which is a function of pulse shape (eg. 0.94 for a Gaussian distribution).

3.3 Achievement of Vacuum and Gas Sample

In order to effectively discriminate the counts of ionized particles being produced in the chamber we need to be able to differentiate m/z values down to approximately 50 counts precision over the course of the observation period which is 1 minute; equating to 60 000 samples. This represents an error tolerance of approximately 0.1%. Above this error rate, it was observed that the systematic effects of system noise and statistical counting errors can combine to prevent the precise measurement required to effectively differentiate between molecules and their fragments. Preventing drift chamber contamination to discriminate the desired molecules is therefore critical to the experiment and can only be achieved at chamber background vacuum levels of 10^{-9} torr and below, as determined via experimentation and observation of error counts. Additionally, above these vacuum levels, it is observed that previous molecules under study will still be resident in the chamber and will alter observed m/z values if their singly or doubly ionized parents and isotopes overlap with the molecules under study or their respective fragments.
The high vacuum is achieved via a two-step process using rough pumps to initially bring the pressure down to 10^{-3} Torr and then Turbo pumps are used to bring the pressure down to 10^{-9} torr. Pumping the chamber down to this required level of vacuum necessitates at least 24 hours of pumping operation (ideally 48 hours) prior to commencing the experiment. Once the vacuum

pressure has been achieved and is all settings are stable, it is important to monitor the pumps' current regularly to ensure effective operation throughout the experiment.

Aromatic molecules were introduced into the chamber in the gas phase by connecting a test tube into a directional flow control manifold built from copper pipe and valves. The gas is allowed to enter the control manifold under its own vapour pressure given that all the aromatic molecules had significantly higher vapour pressure than 1 atm. By using the directional control piping, the gas is led into the chamber via a flexible PVC hose. As with the drift chamber itself, it is critical that all hose components and related ball valves and fittings be pumped down before introducing new chemicals as these components also contain residual traces of chemicals, either from previous experiments or from the lab atmosphere. A separate rough pump is connected via the control manifold to enable this and a pressure sensing gauge is attached to ensure that the correct gas pressure is attained before shutting the valve leading to the test tube source. From there, two additional valves lead to the entrance of the chamber that are sequentially opened to ensure slow and accurate pressure build up in the chamber.

3.4 Time of Flight (TOF)

A Wiley-McClaren TOF system was used to obtain the mass spectra of the aromatic hydrocarbons under study. The Wiley-McClaren system is based on a pulsed two-grid, double field source with repeller and extractor dimensions optimized for resolution [11]. The repeller and extractor generate E-fields of 2000 V/m and 1000 V/m respectively. These two accelerating regions are followed by a field free drift tube. The applied E-fields direct all ions out of the ionization region and into a drift region which is free of any E-field [11]. A Micro-Channel Plate (MCP) located at the end of the TOF detects the ions. To permit the accelerated ions to reach the detector, there is a slit positioned at the center of the extractor plate. The MCP detects particles that come into contact with it via channel grooves that generate secondary electrons. These electrons are then detected by an anode to then pass the signal to a timing discriminator after pre-amplification [12].

Figure 7 shows the drift chamber and actual setup in the lab:

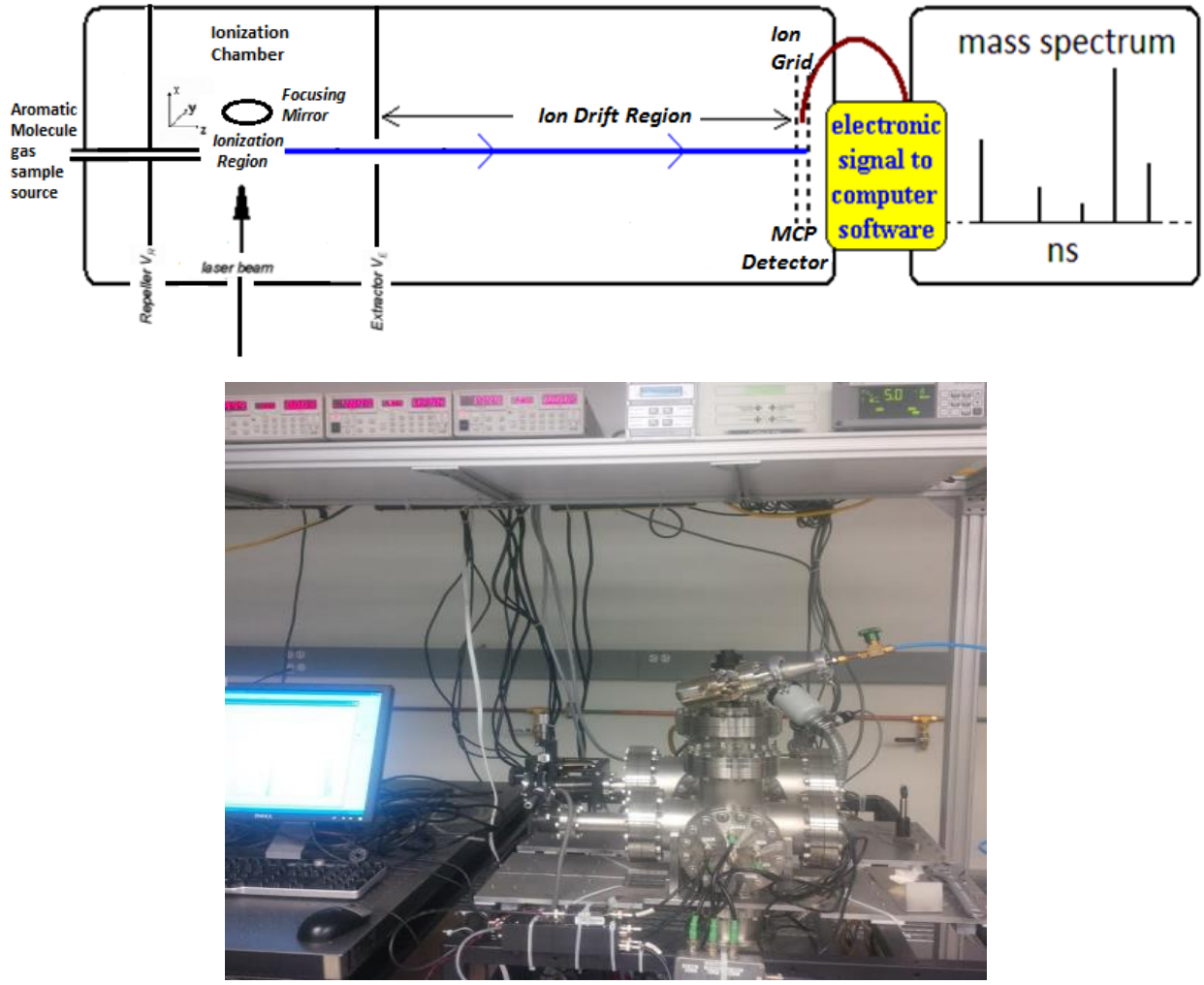

Figure 7: Schematic of drift chamber (top) and actual lab setup photograph (bottom)

Before connecting the MCP detection pulse to the amplifier, discriminator and time digitizer computer circuit card, the pulse was characterized using an oscilloscope. Here we are able to directly observe the characteristic detection pulse at the expected time delay between the laser trigger pulse and the MCP. The expected decaying pulse of the MCP provides the assurance that the correct signal is being transmitted to the software for analysis.

3.4.1 Time Delay Calculation and Data Translation

The time it takes for the ions to travel from the interaction region to the MCP detector is based on the simple relation shown at (3.3) where *l* is the TOF tube length, *V* is the MCP voltage (4900V) and *M/Z* is the mass to charge ratio of the molecule:

$$\boldsymbol{t = l\sqrt{\frac{2V}{M/Z}}} \qquad \textbf{(3.3)}$$

In order to correlate and time sequence the ion impacts at the MCP, a Philips Scientific model #6950 Constant Fraction Discriminator (CFM) is used. The CFM is used to detect the rising and trailing pulses from the MCP as based on the point of zero slope between pulses. These changes are then used by an analog to digital timing generator to obtain intervals relative to the laser trigger. The anode signal from the MCP is amplified via a Philips Scientific amplifier.

3.4.2 Data Capture

The MCP will send a signal of ions detected to a multi-channel time digitizer (a time to digital converter). The input/output ports of the digitizer will relay the ions detections to computer software which captures the total count of ions per a specified time and generates a spectrum. Once the ion detection data is captured, the software will display the time delay on the x-axis and the spectrum in the y-axis. The TOF spectra is calibrated for m/q based on visually identifying known peaks of H_2, O_2 or N_2 which are known to exist in the chamber even at the extreme vacuum levels. Verification of intensity calibration was done by comparing ionization saturation values for molecules such as Ar and Xe gas against known values from the following reference [15].

The intensity at which saturation is reached is determined when the ionization focal area no longer grows proportionately with the ionization count. Saturation can be found be determining the point of intersection between the ionization curve slope and the slope of 3/2. This intersection point is depicted in Figure 8.

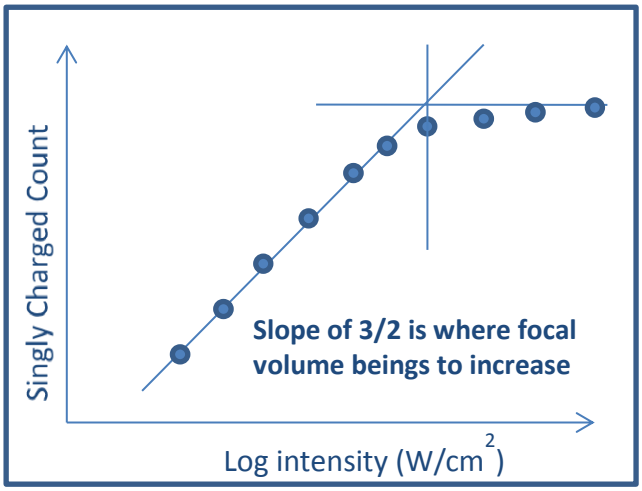

Figure 8: Determining the intensity saturation point as based on the intersection of the two slopes

Determining accurately where this intersection point is can be difficult therefore the saturation point can be extrapolated more readily by using the linear tangent of the log plot of ionization signal count. The point at which this linear tangent intersects the x-axis is taken and compared with literature. This technique was utilized for the current experiment and is shown in Chapter 5. The study of ionization of basic Noble gases such as Argon and Xenon was also to obtain an experimental baseline in preparation for the more complex study of the ionization dynamics inherent in the aromatic hydrocarbons.

Chapter 4: Aromatic Hydrocarbons Experiment

As introduced in Chapter 1, the ionization of molecules under strong field conditions gives us direct insight into their structural, orbital and bond properties. Using these principles and the experimental setup discussed in Chapter 3, this project investigated the ionization and fragmentation of Cyclic Aromatic Hydrocarbon molecules by varying the intensity, polarization (linear, circular & elliptical) and laser wavelength to determine correlation with aromaticity order. The project recorded and analyzed data related to the SI and NSDI in the five member-ring aromatic heterocycles: Pyrrole, Thiophene and Furan.

4.1 Alignment and Optimization

Precise alignment of the beam from the amplification source to the chamber was critical in order to have precise and effective ionization. Alignment was achieved via the placement of 5 iris and aligned in the direction of source to the drift chamber in order to progressively reduce the about of adjustment necessary and to ensure that the most important alignment stages are correct before moving further down the beam line.

As there were three benches in use, one housing the laser, another with the applicable optics and another with the chamber, it was preferable to only adjust alignment on the laser end, ensuring that the incoming beam to the chamber bench arrived in parallel, thereby minimizing alignment in the area that contained most of the sensitive optics.

The setup of optics is illustrated in Figure 9:

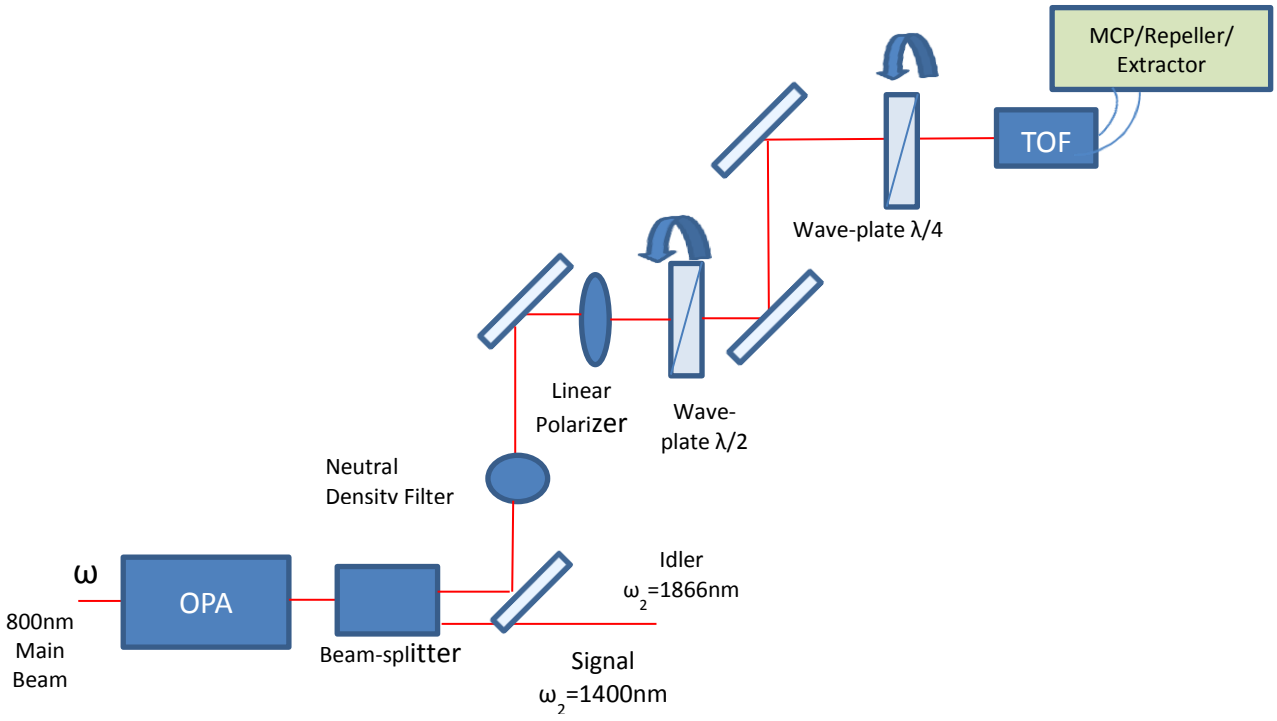

Figure 9: Experimental setup of the laser, optics and drift chamber

Required laser pulses of energies of 1-120 μJ. are aligned to pass through a fused silica window onto a focusing mirror which focuses the beam directly to the centre of the chamber. Via the gas manifold, molecules under study are leaked into the vacuum system. Upon ionization at the centre of the TOF the ions are accelerated and detected by the MCP.

It is also necessary to ensure that the internal chamber mirror is optimally aligned for maximum focusing of the beam on to the molecules for ionization. The internal chamber mirror is mounted on an XYZ axis permitting adjustments in all planes. Control of the axis motion is accessible via knobs at the back of the chamber. Before fine tuning the mirror position, it is necessary to open the drift chamber and align the beam directly to the center of the focusing mirror. The XYZ position of the mirror is fine-tuned for maximum signal strength. Lastly we confirm the alignment by ensuring the back reflection very nearly grazes the main beam.

4.2 Variation of Pulse Energy

The pulse energy and polarization was precisely varied in order to assess the response on ionization and fragmentation dynamics. Accurate energy control was essential to precisely meter the energy entering the drift chamber and to ensure that energy levels are kept under saturation or damage threshold levels.

In order to achieve precise energy control, specific optics were used for coarse and fine energy control. For coarse energy control, a graded neutral density filter wheel was used allowing energy to be reduced to the order of <100 μJ. For precise energy control below 100 μJ, a Half Wave Plate (HWP) and polarizer were used in conjunction. While the neutral density filter wheel could hypothetically reduce energy down to the levels required, the HWP/polarizer combination was used instead as this method offered a more linear and consistent graduation in energy and greater precision control. To understand this methodology specifically; the HWP rotates the incoming polarization (by 2θ). Therefore, as the polarization direction of the linearly polarized light is rotated, only the E-field vector that is aligned with the polarizer can be transmitted. By adjusting the propagation of this variable linear component which matches the polarizer's direction, precise control is obtained. For example, when the polarizer's plane of transmission is precisely orthogonal to the beam, transmission can be completely cut off.

4.3 Polarization Control

To convert the polarization from linear to circular, a Quarter Wave Plate (QWP) was used. To calibrate the QWP to the desired polarization, the maximum energy (Emax) and minimum energy (Emin) of the beam was measured via a polarizer for a given position of the QWP. At the QWP position that provided a maximum value of the Emin/Emax ratio (greatest spread between Emax and Emin), linear polarization is obtained. At the minimum ratio value (Emax and Emin almost equalling each other), we obtained circular polarization. Theoretically the maximum ratio of Emax over Emin should equal 1 and the minimum ratio should equal 0 however these values

cannot be practically achieved. Elliptical polarization was attained at intermediate values of the Emin/Emax ratio.

4.4 Wavelength Variation

In order to verify consistency of results across wavelengths, the photoionization experiment was carried out at 800nm and using the Optical Parametric Amplifier (OPA) output at 1866nm (Idler) and at 1400nm (signal). The variation of wavelength varies the properties of the laser strong field resulting in greater probability of either photoionization occurring from the tunnelling or multi-photon regimes. Recalling equations 1.7 and 1.8 from Section 1.4.4 (Keldysh Parameter), we see that an increasing wavelength has the proportional effect of increasing the ponderomotive potential which in turn is inversely proportional to the Keldysh parameter γ.

$$U_P = {e^2E^2}/{4m\omega^2} \quad \textbf{(4.1)}$$

In this case, increasing the wavelength from 800nm to 1866nm increases the likelihood of tunnelling as the frequency has a direct relationship with tunnelling time. Table 2 shows calculated values for the Keldysh parameter γ indicating that at 1866nm, ionization is almost purely from tunnelling.

Intensity (W/cm^2)	Wavelength	
	800 nm	1866 nm
1×10^{13}	2.8	1.0
5×10^{13}	1.3	0.5
1×10^{14}	0.9	0.4
5×10^{14}	0.5	0.2
1×10^{15}	0.3	0.1

Table 2: Calculated Values for Keldysh parameter γ shows that at 800 nm we expect MPI while at 1866nm we expect predominantly tunnelling

By changing the dynamics of photoionization into a preferential tunnelling regime, we are ensuring that our results are not specific to MPI. Furthermore, at 1866nm, the polarization dependence of NSDI is increased given the longer frequency and therefore time duration that electron wavepacket spends in the laser field. The longer the wavepacket spends in the laser field the greater it is affected by it. Comparison of the ionization results at both wavelengths therefore provides an opportunity to compare these effects in relation to aromaticity.

4.5 Discriminating TOF Peaks

When dealing with large molecules, the spectrum of ionized particles can be particularly complex and difficult to discern accurately if using mass to charge ratio only. It is crucial therefore that peaks are properly discriminated, firstly by conducting accurate mass calibration and secondly by validating the exact ratio of parent molecules to their respective isotopes such that singly and doubly charged parent ion peaks can be positively identified.

4.5.1 Mass Calibration

To permit detailed analysis of the ion spectra, molecular mass spectra must be calibrated from raw TOF values to expected amu values. Given that precise beam alignment in the x,y and z-axes are normally adjusted at the time of experiment to maximize ion yield, the precise distance from the TOF ionization point to the MCP detector varies and must therefore be compensated in the conversion of flight time to m/z. Mass calibration is therefore achieved using known mass spectra obtained from reference [15]. Atoms, such as Xenon are used for calibration as their ionization spectra are precisely known and stable doubly and triply ionized parent permit accurate calibration.

The mass spectrum for Xe is shown in Figure 11 with the parent ion at 132 amu and related isotopes highlighted. Doubly charged Xe is also visible at m/z 66 amu.

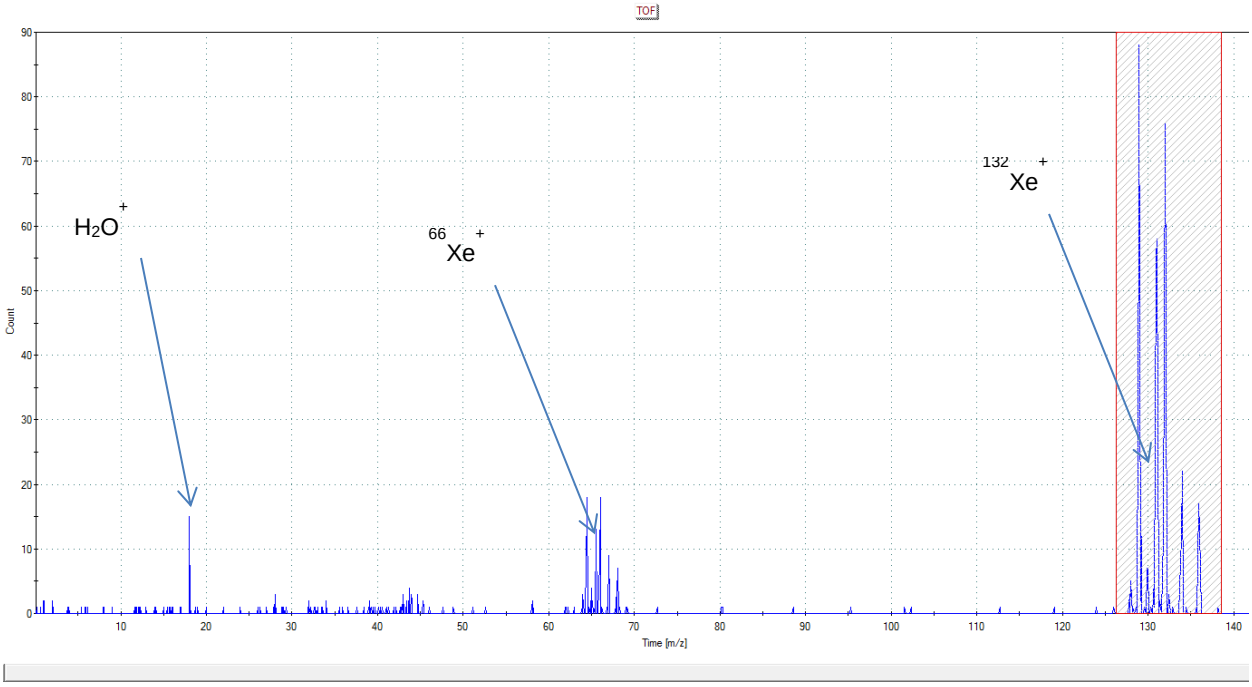

Figure 10: Mass spectra for Xe taken at 15 μJ, 4.2 x 10^{-8} Torr shows the presence of singly and doubly charged ions. The presence of molecules such as water permits mass calibration.

Following mass calibration, parent ions are confirmed by comparing predicted quantities of isotopes and related fragments with reference.

4.5.2 Confirmation of Parent Ions

For atoms and molecules, the relative abundance of the respective isotope ions to parent ions on the TOF mass spectrum permits us to discriminate directly the parent ions of interest since the relative abundances are known from reference.

The mass spectra for Thiophene is provided in Figure 12 as an example of parent ions and their isotopes for both singly and doubly charged ions:

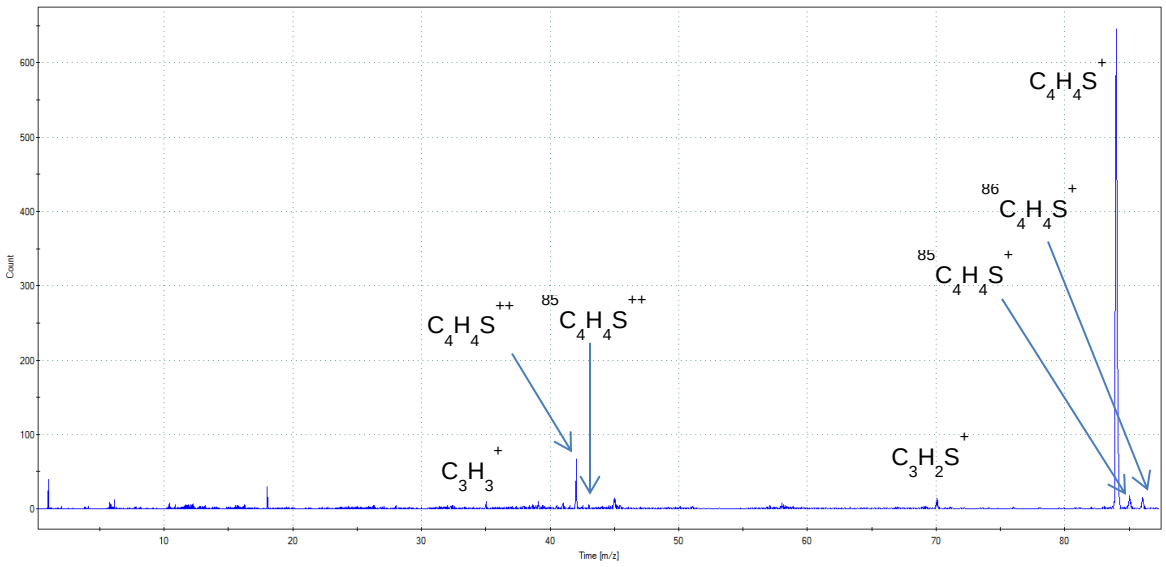

Figure 11: Mass spectra of Thiophene taken at 20 µJ, 4 x 10^{-8} Torr shows the presence of singly and doubly charged molecules together with their isotopes.

Comparing experimental data to reference, the parent-isotope ratio is plotted as a function of intensity and a best fit is applied for both singly and doubly charged ions and for all molecules. The plot of the ratio as a function of intensity provides an indication of consistency but also of saturation effects and also to verify that there is no contribution of fragmentation at the same m/z. An example of this is illustrated in Figure 12 for Thiophene using it's doubly charged parent-isotope ratio. In this case, we predict the doubly charged peak location on the mass spectrum as based on its increased acceleration and the molecule reaching the detector in half the time. Within the non-saturated region presented in Figure 12, we see that constant ratio of 0.05 correctly shows the relative abundance of Thiophene (^{84}C4H4S) to its isotope (^{85}C4H4S) as taken from reference [14].

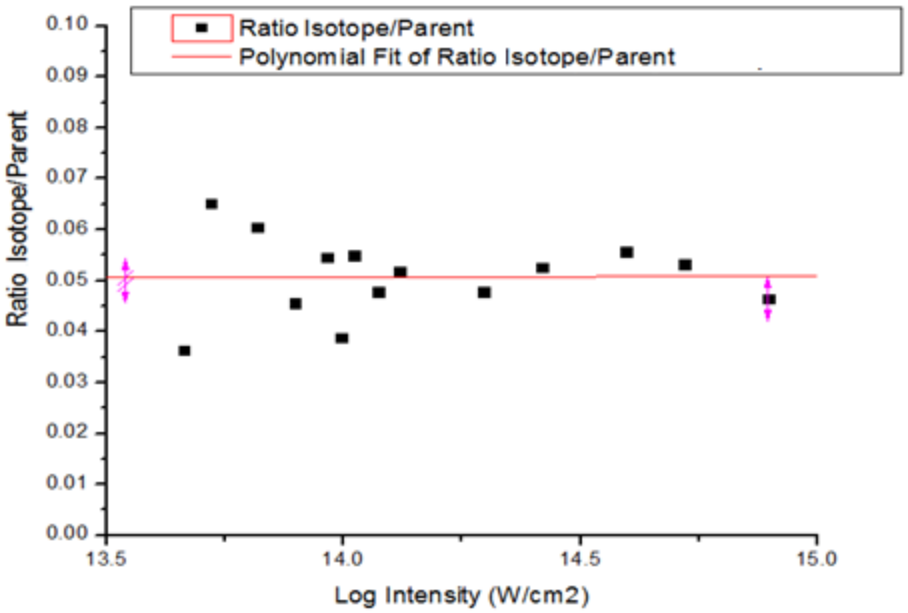

Figure 12: Parent-Isotope ratio plotted as a function of intensity shows consistency at higher intensities.

After validating the parent ion peak via its isotope, the correct quantity of parent ion must also be validated by verifying the possible presence of fragments at the same mass to charge ratio. This was less likely the case for singly charged molecules in comparison to doubly charged where the smaller mass over charge ratio is comparable to that of several possible fragments. Normalized values of parent peaks may also be discerned by using the isotope ratio from reference to plot them as a function of their isotope levels obtained from the mass spectrum.

Chapter 5: Photoionization of Aromatic Molecules

5.1 Intensity Calibration

Particular attention needs to be placed when measuring the ionization rate of molecules in the high-intensity regime due to the uncertainty of the absolute intensity. Therefore, we need to precisely know the intensity at which the ionization results are obtained so that comparisons can be made amongst molecules. In order to accomplish a comparison of molecular ionization rates, the laser intensity must therefore be calibrated for consistency. This is additionally important due to the unique laser setup conditions and daily adjusted alignment which results in the amount of energy required to saturate a molecule to vary at the time of experiment.

By comparing the saturation energy obtained by experiment to the known value from literature (for Xe we use 1.2 x 10^{14} W/cm^2), we can calibrate our laser energy to an accurate and consistent intensity level. The saturation point is specifically obtained by taking the x-axis intercept value of the linear fit to the saturation curve for Xenon. Figure 14 shows an example of saturation intensity obtained for Xe:

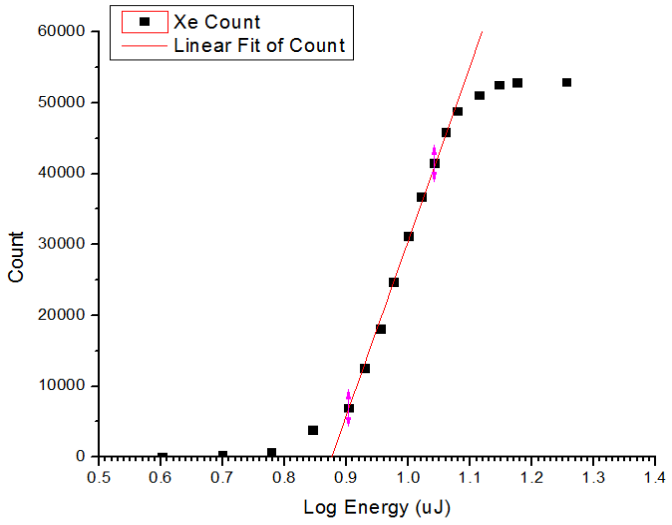

Figure 13: Saturation Intensity for Xe at 800 nm, 4.4 x 10^{-8} Torr. Shows the linear fit to the semi-log curve with x-axis intercept. Inverse-log of intercept value provides saturation point and is used for intensity calibration.

Noting the saturation intensity value from literature and taking the inverse log of the saturation energy from the above curve, we can calibrate the intensity accordingly. The linear fit to the semi-log plot is taken between the points that have the least uncertainty between them as indicated by the bars on the graph. In this particular case, 7 points are used for the linear fit and the x-axis intercept provides the saturation point. This curve intercept corresponds to an energy of 7.3 μJ when the inverse log is taken. This value is then used as a ratio with the energy being applied and then multiplied by the intensity value from literature to obtain a calibrated intensity.

Qualitatively speaking, saturation can also be noted visually from the mass spectrum by noting the deformations at the base of the parent ion peak due to inconsistent ionization in the focal volume and thus variations in the m/z due to varying ion trajectories. An example of this is shown in Figure 15 for Furan and varying intensities:

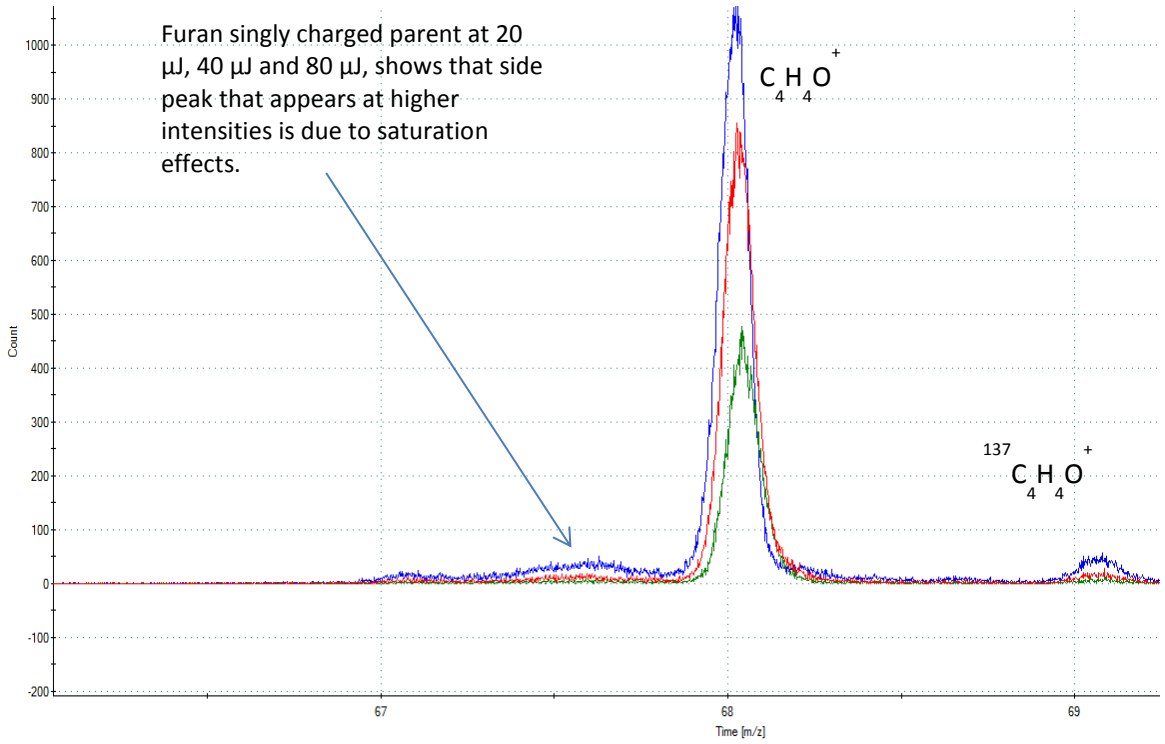

Figure 14: Qualitative saturation observations provide a visual indication of saturation as singly charged ions are no longer ionized proportionately in the focal volume.

5.2 Aromatic Molecule Saturation Intensities

The linear fit to the saturation curve is predictable due to the asymptotic nature of saturation as based on the ionization focal area of the beam as energy increases. Prior to saturation, the proportion of ionized molecules contained within the focal volume grows proportionally with laser intensity however this is eventually maximized. The intensity at which this maximum occurs is unique for molecules and is therefore an important characteristic in the analysis of the ionization dynamics. The intensity level where the focal volume is maximized is an indicator of the molecule's propensity to ionize with lower saturation intensities correlating with higher ionization yield.

Sections 5.2.1 to 5.2.4 show the saturation intensity curves for the molecules under study at 800 nm and 1866nm at both linear and circular polarization. Figures 16 to 19 have a linear fit that is obtained by selecting the broadest set of points that provides the least uncertainty. The Chi-squared value is used to assess the uncertainty value enabling us to select the optimal points for fitting purposes.

5.2.1 Plot 800nm, Linear Polarization

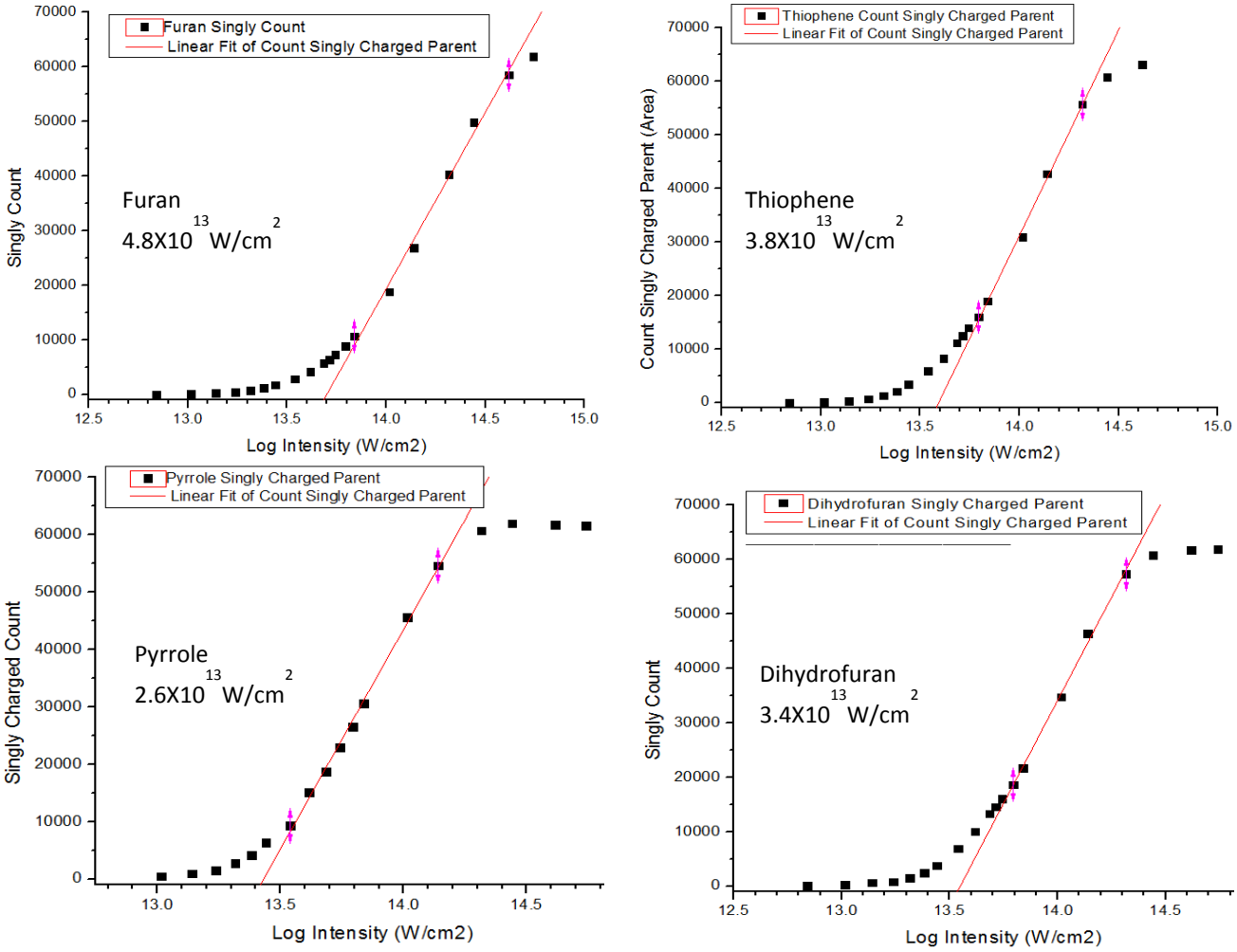

Figure 15: Saturation intensity curves at 800nm, Linear Polarization.

The saturation intensity order of the aromatic molecules using linear polarization is as follows (in order of increasing intensity): **1. Pyrrole, 2. Thiophene, 3. Furan**

Lower saturation intensity in Pyrrole permits us to conclude that the molecule requires less laser intensity in the focal volume to ionize a given number of molecules. This correlates to the π orbital electron delocalization inherent in aromatic molecules. Results suggest Pyrrole is more aromatic followed by Thiophene and then Furan.

5.2.2 Plot 800nm, Circular Polarization

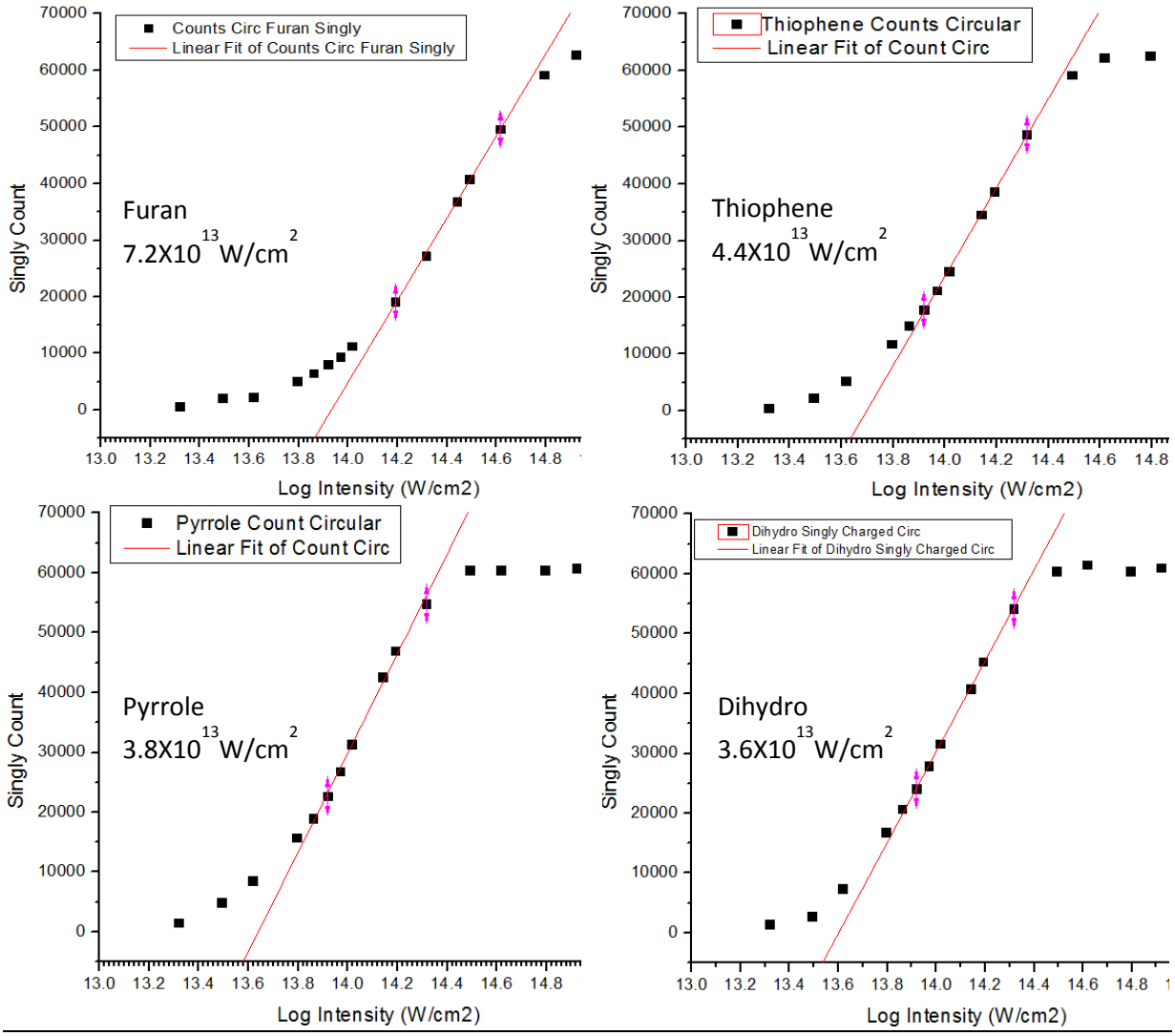

Figure 16: Saturation Intensity curves at 800nm, Circular Polarization

The saturation intensity order of the aromatic molecules using linear polarization is as follows (in order of increasing intensity): **1. Pyrrole, 2. Thiophene, 3. Furan**

Similar to the case of linear measurements taken at 800nm, the results for circular polarization demonstrate that Pyrrole is more aromatic than Thiophene and Furan.

5.2.3 Plot 1866nm, Circular Polarization

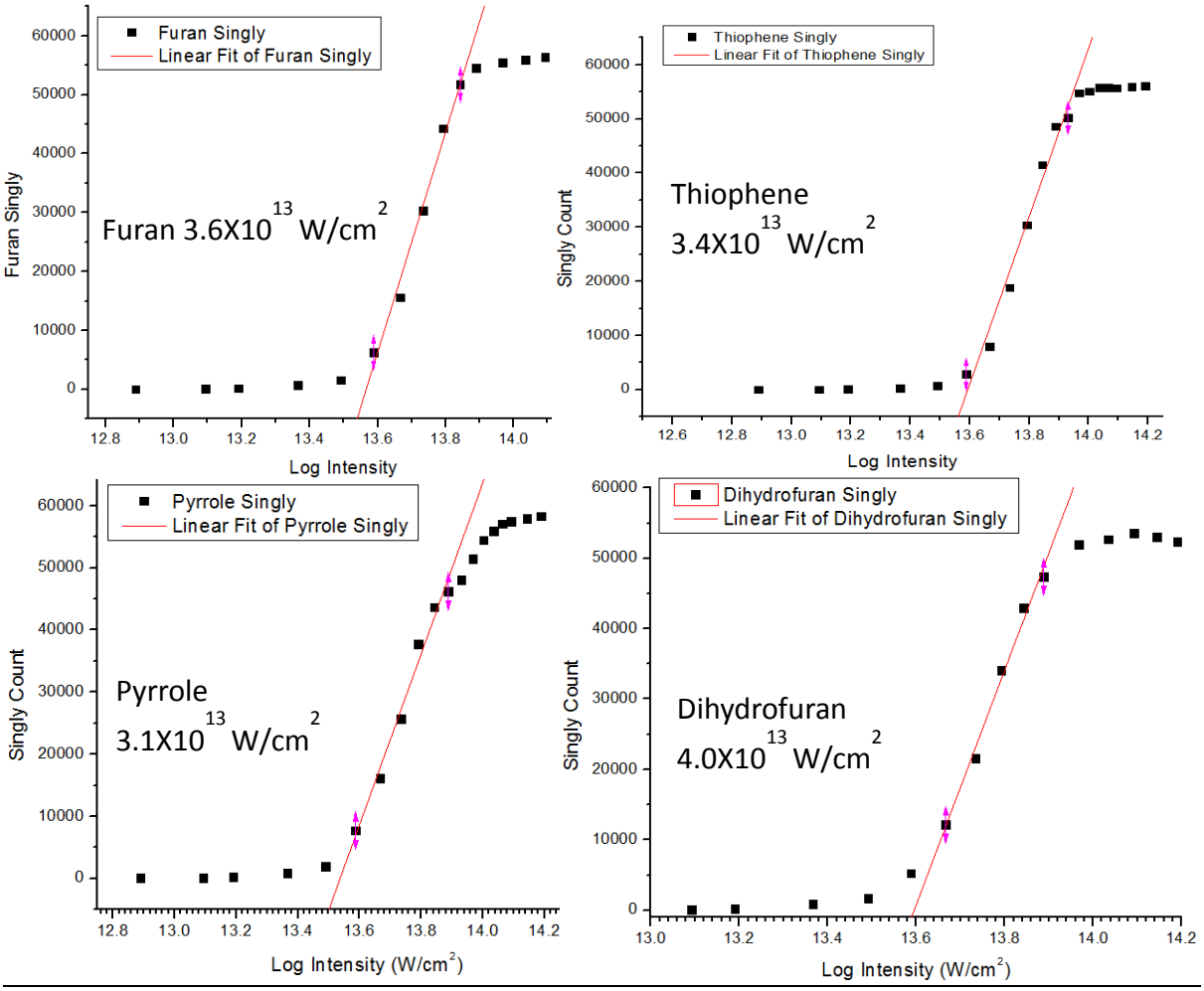

Figure 17: Saturation Intensity Curves 1866nm, Linear Polarization.

The saturation intensity order of the aromatic molecules is as follows (in order of increasing intensity): **1. Pyrrole, 2. Thiophene, 3. Furan**

Similar to the linear polarization results taken at 800nm, the results at 1866nm demonstrate consistency in Pyrrole being more aromatic than Thiophene and Furan. With greater effects from tunnelling expected at 1866nm, this result shows that the greater ionization stability resulting from the delocalized electron structure is consistent under varying ionization conditions.

5.2.4 Plot 1866nm, Circular Polarization

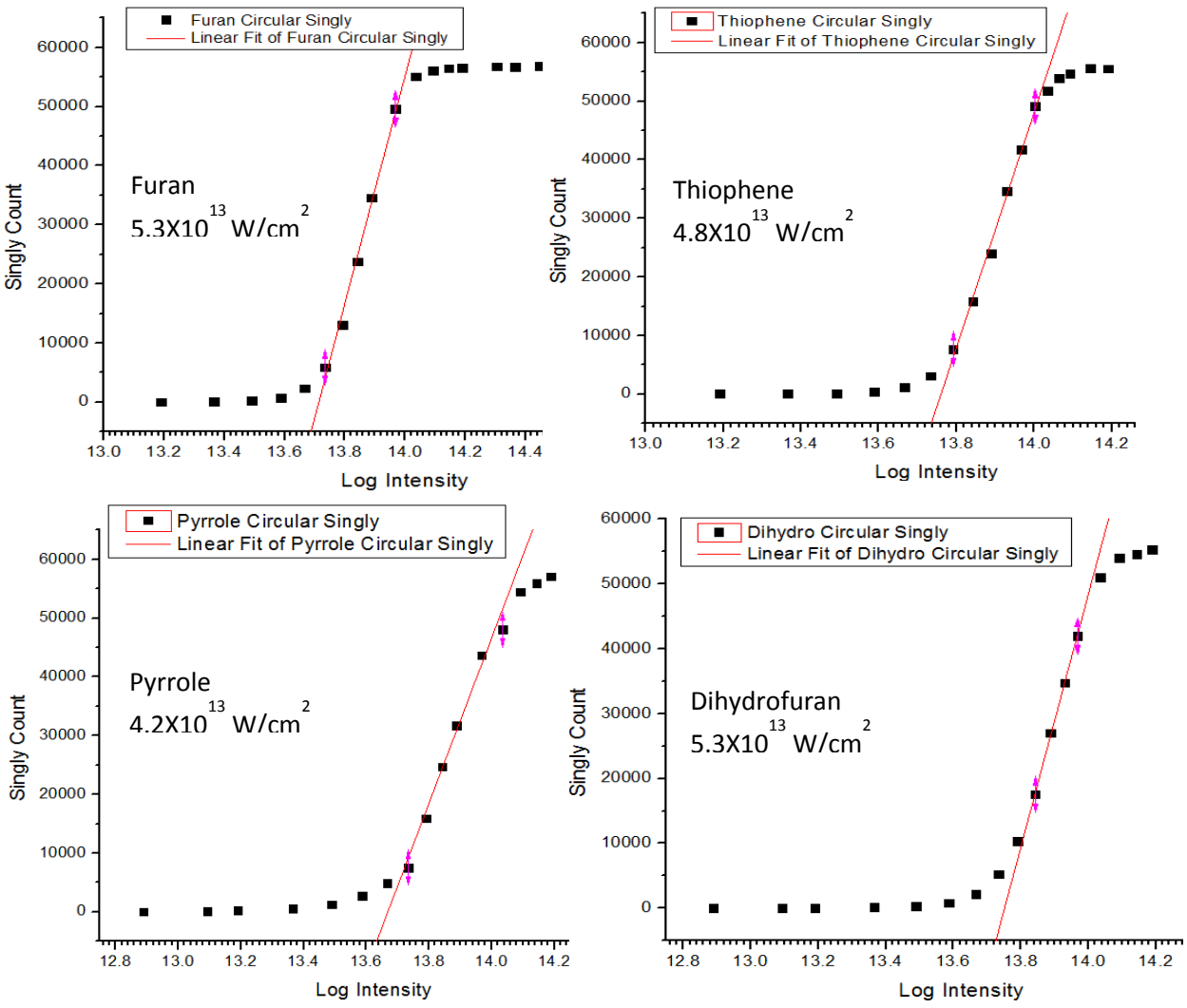

Figure 18: Saturation Intensity Curves 1866nm, Circular Polarization

The saturation intensity order of the aromatic molecules is as follows (in order of increasing intensity): **1. Pyrrole, 2. Thiophene, 3. Furan**

From the above saturation curves, it is noted that the order of saturation intensity remains consistent at both 800nm and 1866nm and using both linear and circular polarization. Of the aromatic molecules, Pyrrole has the lowest saturation intensity and given the above observations we can postulate that it has the highest aromatic properties in comparison to Thiophene in 2nd place followed by Furan.

5.3 Polarization Variation:

Laser ellipticity is defined as the ratio of x and y components of the electric field, namely $\varepsilon = E_y/E_x$. Variation in polarization provides insight into the traverse electron momentum of the tunnelled electron wavefunction. This is because as the electron wavepacket, aside from spreading from quantum uncertainty, will have an initial transverse velocity. While propagating in the oscillating field, the electron wavepacket will return to the parent ion resulting in possible recollision depending upon this transverse momentum. Linear polarization provides the maximum probability for recollision as the wavepacket is brought directly back upon the parent molecule. As ellipticity increases, the electron wavepacket is increasingly brought further away from the ionization centre point. When circular ionization is reached, the electron wavefunction completely misses (exceeds the molecular ion's radius) since E_x and E_y are equal and hence recollision does not occur. This analysis therefore provides us important insight in regards to the electron wavepacket momentum as we analyze the yield of NSDI as a function of ellipticity. A visualization of this is provided in Figure 20 for a Noble gas atom, such as Argon.

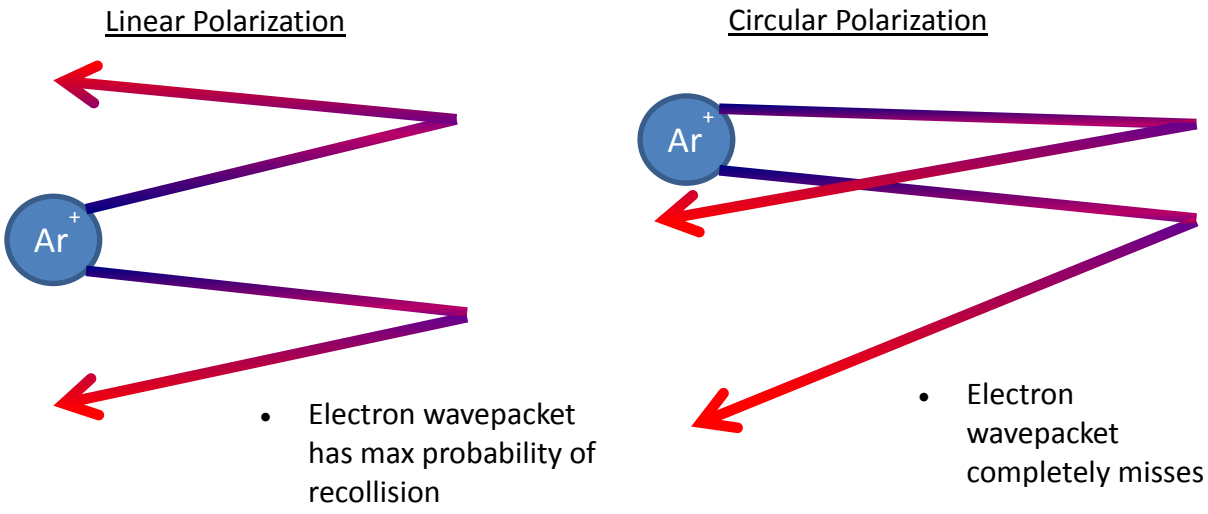

Figure 19: Visualization of electron wavepacket momentum spreading in an oscillating laser field and effect of polarization on the probability of recollision

The process of studying ellipticity is critical in providing insight to the electron wavefunction spreading after tunnelling in relation to the parent ion and therefore its effect on recollision probability. In the case of aromatic molecules, the wavepacket spreading of the delocalized

electrons contained within the π orbitals will depend on molecular structure and aromaticity as will be see in this Section. Firstly, the comparison of linear to circular polarization is addressed in Section 5.3.1

5.3.1 Photoionization with Linear and Circular Polarization

Besides the fact that electron wavepacket completely misses the parent ion in circularly polarized light, photoionization by linear and circular polarized light can be different. For example, the E-field of linearly polarized light will be greater than the circular polarization E-field, that is $E_{linear} > E_{circular}$. This is because the E-field amplitude for circular polarization is smaller than that for linear by a factor of $\sqrt{2}$ (reduction to approximately 0.71×10^{14} W/cm^2).

On the other hand, in the tunnelling regime which is wavelength dependent, for a given pulse energy we expect the tunnelling probability to be greater for circular than linear. This is because of the oscillatory nature of the circular polarization field which is considered to be on at all times resulting in increased probability of tunnelling. Therefore by studying the variations obtained in singly ionization count of linear and circular polarization we gain insight into the intensity dependence for ionization, namely the effects of ionization potential of the atom or molecule to the laser intensity being applied.

Ionization of an atom/molecule results in slightly different yields for a given intensity with use of linearly and circularly polarized light. So, to obtain similar yields for both laser polarizations the intensity of circular polarized light has to be adjusted by a scaling factor that arises from the two opposing effects discussed above. For atoms, the scaling factor is 0.65.

Figure 21 shows the linear to circular polarization horizontal axis shift for the aromatic molecules.

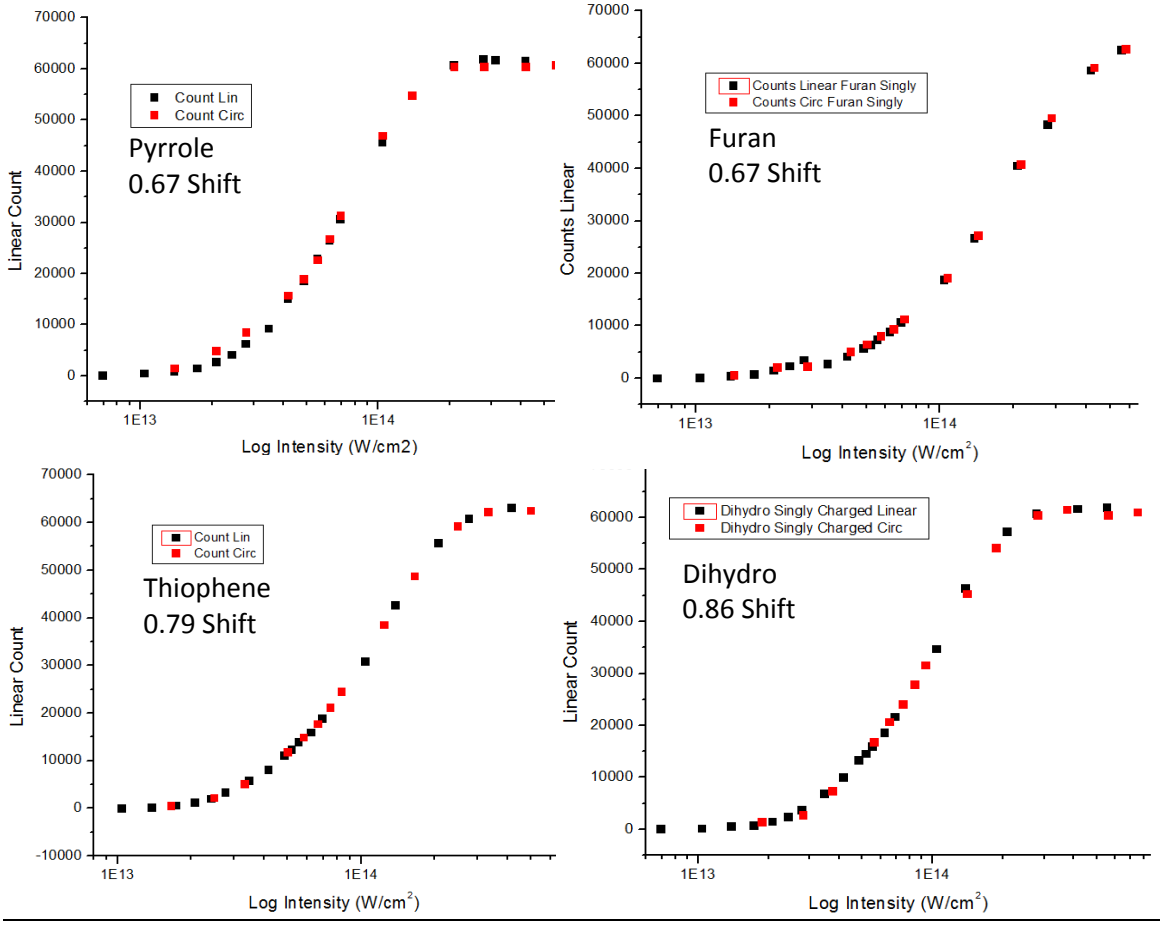

Figure 20: Degree of shift in linear vs. circular ionization results

The aromatic molecules under study show that for a specific intensity, the singly charged count for circular polarization is lower for all molecules. The intensity scale (x-axis) is shifted by a factor of 0.67 for Pyrrole and Furan and by 0.79 for Thiophene and 0.86 for Dihydrofuran. Higher scaling factors in some molecules compared to Xe (0.65) highlights the differences in tunnel ionization among different species.

5.3.2 Elliptical Polarization Variation

The tranverse spread of the tunnelled electron wavefunction measured by varying the laser polarization gives us insight into the electronic structure of the molecule. We can discern this based on the variation of doubly charged ions resultant from Non-Sequential Ionization normalized to the singly charged count. In order to compare the aromatic molecules under study, it is important to first compare and understand the response for atoms such as Ar gas. For these atoms, ellipticity is expected to have a Gaussian distribution (FWHM=0.186 for Ar data) with a maximum at linear polarization, falling off sharply as ellipticity is increased toward a value of 1 as seen in Figure 22:

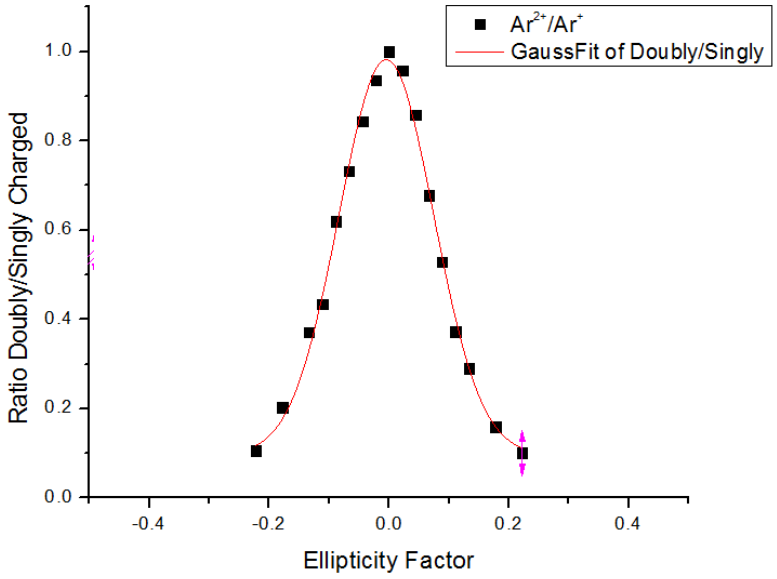

Figure 21: Non Sequential Doubly Ionization as a function of ellipticity shows a narrow Gaussian distribution resulting from low electron wavepacket momentum

Comparing the result for Argon gas to the aromatic molecules, the intent moving forward in the analysis is to understand how the transverse spreading of electron wavefunction will vary when associated with the unique electronic structures and orbital properties of aromatic molecules. For the molecules, the normalized doubly charged ion yield ($M^{2+/}M^{+}$) was obtained at 5 μJ, 7 μJ and 9 μJ. These lower intensities were chosen to minimize saturation effects. The Full Width at Half Maximum (FWHM) is taken as a consistent point of measurement for assessing the transverse spreading of the electron wavepacket.

5.3.3 Elliptical Polarization Variation at 9 μJ

In Figure 23, results were taken from -45 to +45 QWP angle producing -1.0 to 1 ellipticity change. Measurements extrapolated from Figure 23 plots are transposed to Table 3 for ease of comparison:

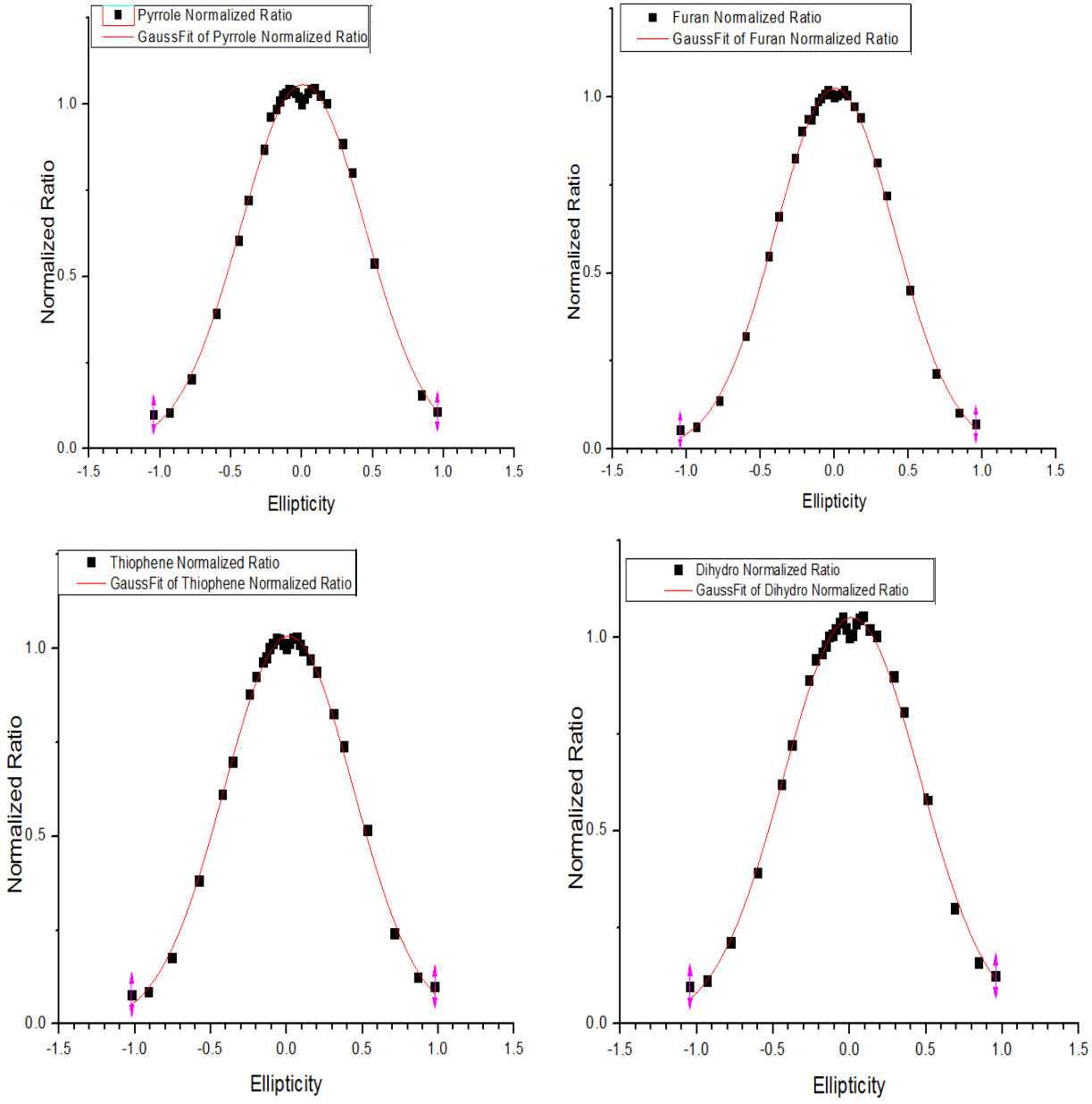

Figure 22: Ellipticity results at 9uJ, 1866 nm shows Gaussian curve broadening in comparison to the Argon Noble gas molecule.

Molecule	R^2	FWHM	Chi Squared
Pyrrole (upper left)	0.995	1.034	6.14×10^{-4}
Furan (upper right)	0.998	0.947	2.05×10^{-4}
Thiophene (lower left)	0.997	1.006	3.07×10^{-4}
Dihydrofuran (lower right)	0.995	1.053	5.29×10^{-4}

Table 3: FWHM values for ellipticity dependence of NSDI at 9 μJ shows that Pyrrole has greatest broadening effect

While the ratio of M^{2+}/M^{+} ratio drops off to zero as expected at circular polarization, the increase of curve broadening gives us an indication of the degree to which the transverse electron wavefunction continues to interact with the molecular ion as it is increasingly shifted away from the its point of ionization.

The measurements of FWHM shown in Table 3 indicated that the order from greatest to least broadening of the aromatic molecules is:

1. **Pyrrole (1.034), 2. Thiophene (1.006), 3. Furan (0.947)**

Interpretation of broadening in this particular order can be attributed to the greater amount of π-orbital delocalization. Greater the electron delocalization in a molecule, larger is the transverse spreading of the electron wavepacket upon ionization and hence weaker ellipticity dependence (larger FWHM). This enhanced re-collision ionization is demonstrated in the ellipticity curve broadening and can therefore be an indirect measure of aromaticity order. The FWHM result for Dihydrofuran is 1.053 which is greater than the 3 aromatic molecules however it is not possible to compare this result directly with the other aromatic molecules given that Dihydrofuran is not aromatic.

5.3.4 Elliptical Polarization Variation at 7 μJ

Similar to the measurements taken at 9 μJ, the results at 7 μJ are shown in the plots of Figure 24 and summarized in Table 4:

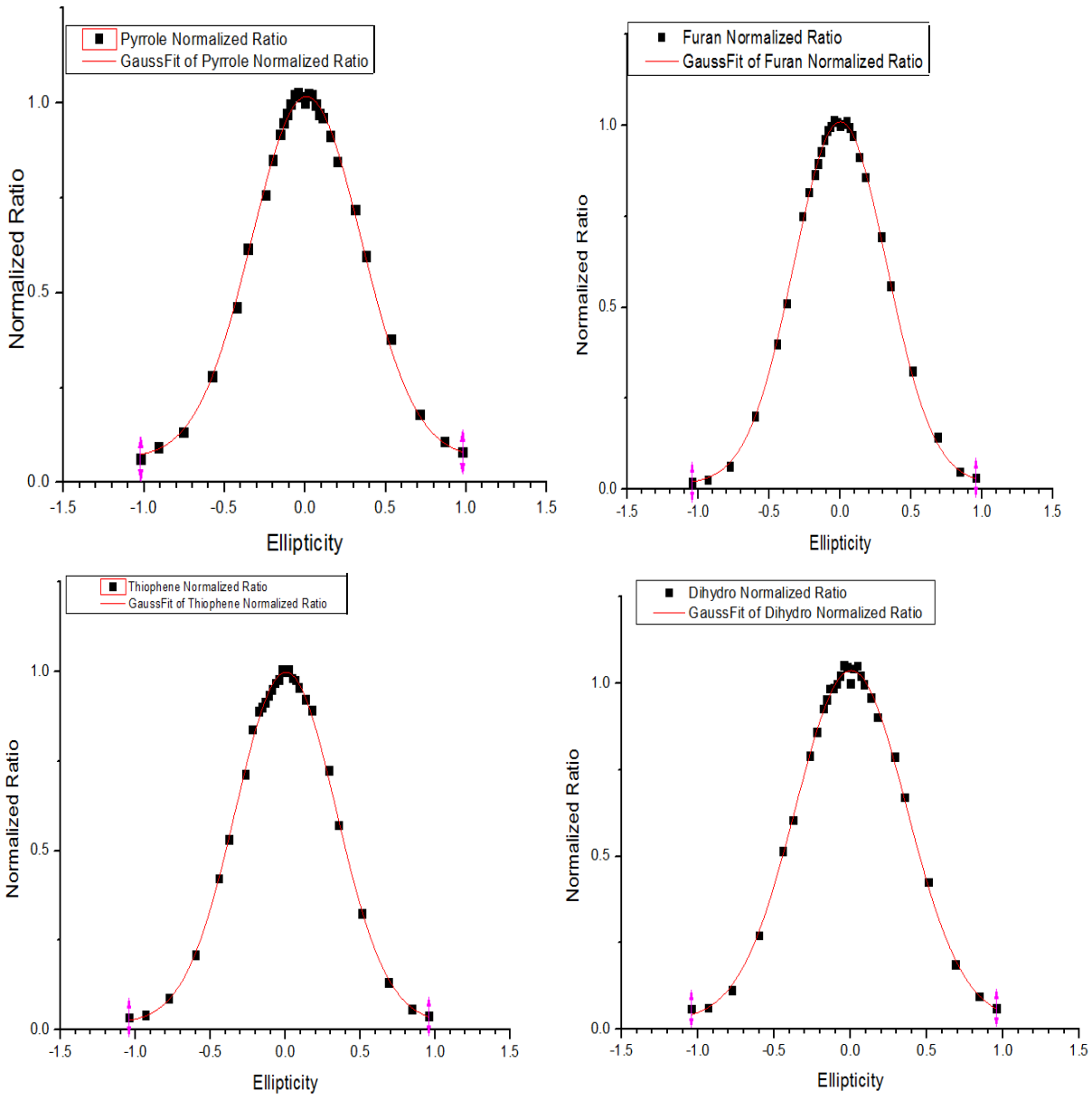

Figure 23: Ellipticity results at 9uJ, 1866 nm shows Gaussian curve broadening in comparison to the Argon Noble gas molecule.

Molecule	R^2	FWHM	Chi Squared
Pyrrole (upper left)	0.998	0.799	2.88×10^{-4}
Furan (upper right)	0.999	0.770	1.31×10^{-4}
Thiophene (lower left)	0.999	0.791	1.76×10^{-4}
Dihydrofuran (lower right)	0.998	0.859	2.35×10^{-4}

Table 4: FWHM Values for ellipticity dependence of NSDI at 7 μJ shows that Pyrrole has greatest broadening effect, consistent with measurements taken at other intensities.

The order of FWHM measurements shown in Table 3 are as follows:

1. **Pyrrole (0.799), 2. Thiophene (0.791), 3. Furan (0.770)**

As with the results at results taken at 9 μJ, the FWHM value for Dihyrdofuran (0.859) is greater than the 3 aromatic molecules however direct comparison should not be made given the non-aromatic characteristics of this molecule.

The order of curve broadening as measured at FWHM at 7 μJ is consistent to that taken at 9 μJ and at other energies that were taken in the lab. This confirms that the broadening results are not intensity dependent and we can surmise the important features of transverse momentum spreading as a function of ellipticity.

5.3.5 Ellipticity Curve Peak Offset

As shown in Figures 22 and 23, it is observed that the ellipticity curves exhibit a relative dip at the origin. It is assessed that this is the result of destructive interference occurring due to simultaneous ionization from upper and lower orbitals. Figure 24 depicts this offset with an arrow (blue) showing the dip at the origin and arrow (red) showing relative maximum:

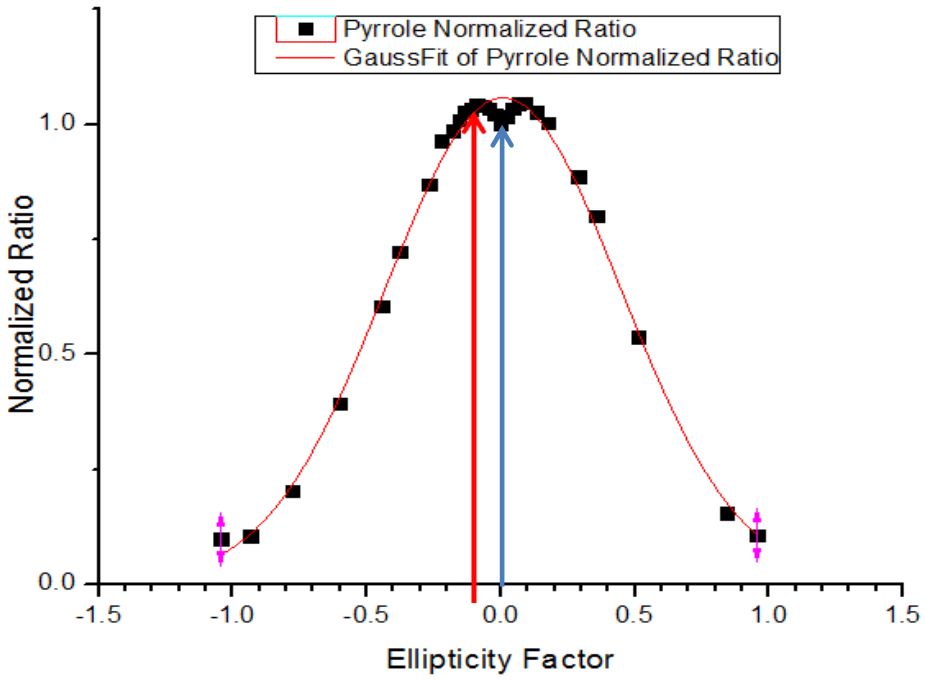

Figure 24: An offset in the ellipticity dependent curves is the result of destructive interference

As noted in Sections 5.3.3 and 5.3.4, the offset is different for each of the aromatic molecules. It is observed that the amount of offset is greatest in Pyrrole followed by Thiophene and Furan. The degree of ellipticity factor (ε) offset to the maximum value of normalized $M^{2+/}M^{+}$ is shown in Table 5 for the aromatic molecules.

Molecule	ε value at max
Pyrrole	**0.08**
Thiophene	**0.07**
Furan	**0.06**
Dihydro-furan	**0.07**

Table 5: Degree of offset for the aromatic molecules under study.

These differences are the result of destructive interference from simultaneous ionization from upper and lower orbitals. Greater ellipticity permits a shift in the ionization direction thereby eliminating this interference. The amount of offset gives us insight into the orbital extent of the upper and lower lobes. The greatest offset noted in Pyrrole followed by Thiophene and then Furan gives us additional knowledge of how orbital extent may play a role in electron delocalization of aromatic molecules.

In summary, the ellipticity $M^{2+/}M^{+}$ curves provide us insight into the correlation between the transverse spread of the electron wavefunction and the π orbitals of the aromatic molecules. Therefore, the hypothesis that aromatic molecules whose π orbitals result in the enhancement of electron delocalization can be further confirmed by the order of curve broadening.

5.4 Photoionization and Aromaticity

The singly, doubly and normalized ionization plots provide insight into the ionization dynamics of the aromatic molecules. Two separate data sets were collected for both 800 nm and 1866 nm wavelengths shown in Figures 26 and 27. Data derived from these results was found to be internally consistent at each wavelength and when comparing 800nm to 1866nm (OPA Beam). The results suggest that photoionization rates are sensitive to the aromatic nature of the molecules. Error-bars are for the respective plots are smaller than the pixel size hence are not displayed.

5.4.1 Singly Charged Ionization

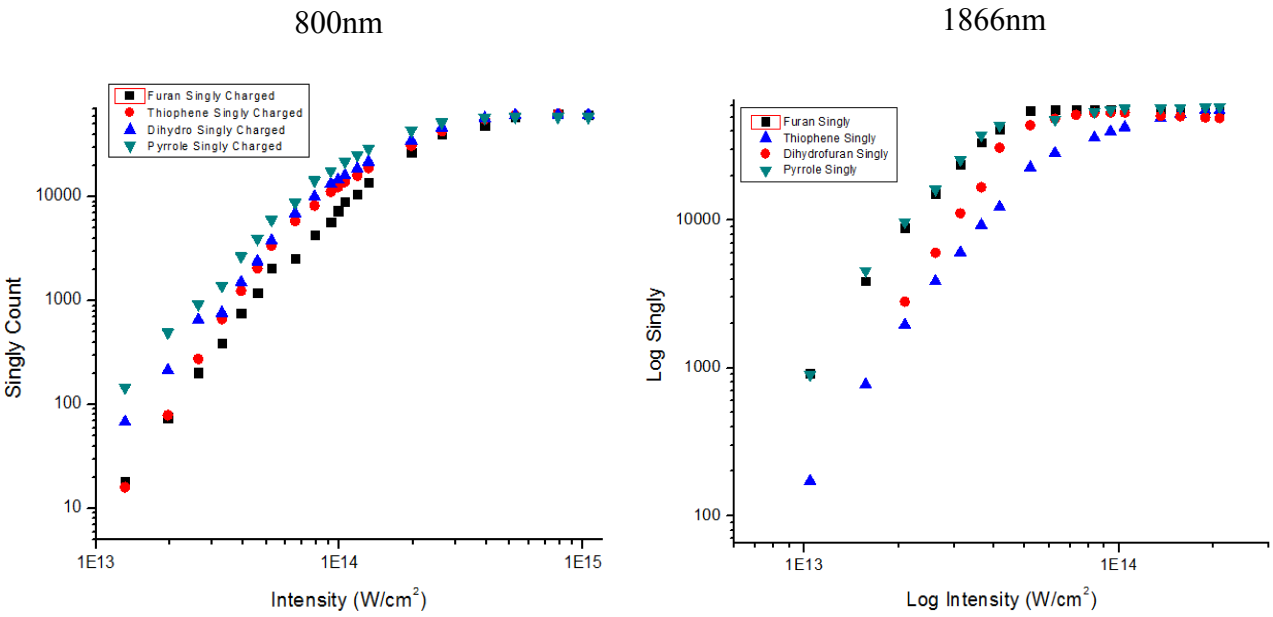

Figure 25: Singly charged ion count as a function of intensity in a log-log plot shows the relative ordering of aromatic molecules.

For the aromatic molecules the order of singly ionization rate from highest to lowest, in the non-saturated region is: **1) Pyrrole, 2) Thiophene, 3) Furan** at 800nm and;

1) Pyrrole, 2) Furan, 3) Thiophene at 1866nm.

We note a change in the order between Thiophene and Furan at 1866nm. With a change to longer wavelengths we have an increased probability of tunnelling ionization. It is possible to surmise therefore that at 1866nm, Furan shows greater tunnelling ionization than Thiophene. From the ordering results, we can also conclude that Pyrrole ionizes more readily than Furan and Thiophene suggesting that it has greater aromatic properties of stability and enhanced electron delocalization.

5.4.2 Doubly Charged Ionization

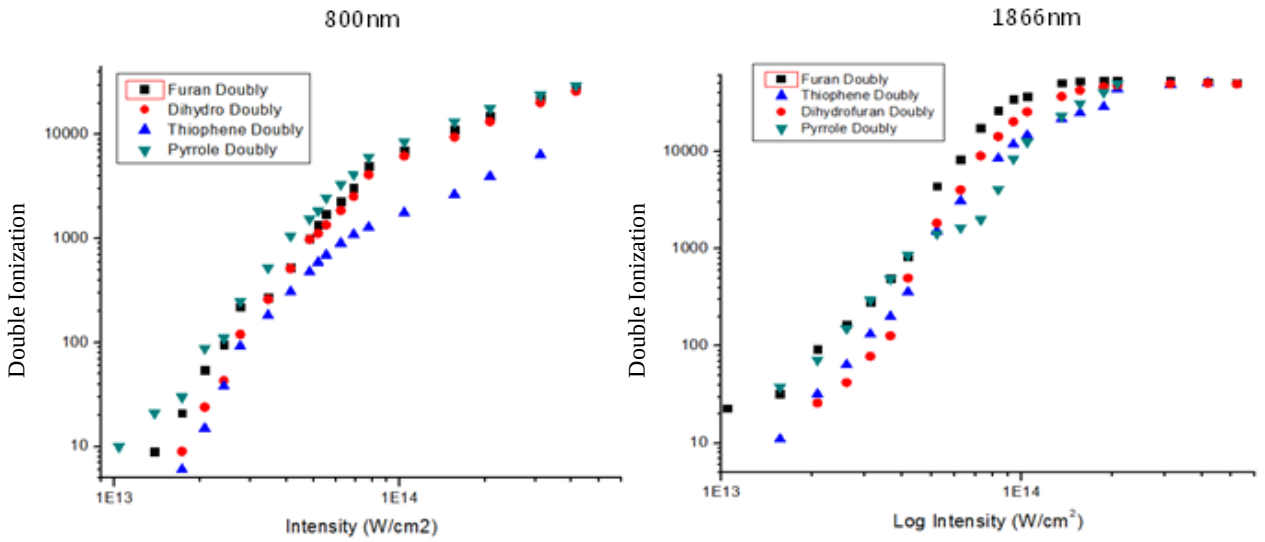

Figure 26: Doubly charged ion count as a function of intensity in a log-log plot shows the relative ordering of aromatic molecules.

For the aromatic molecules the order of doubly ionization rate from highest to lowest, in the non-saturated region is:

1) **Pyrrole, 2) Furan, 3) Thiophene** at 800nm.

As with singly charged ionization yield, for doubly charged at 800nm we can conclude that Pyrrole ionizes more readily than Furan and Thiophene supporting the assessment that Pyrrole has greater aromatic properties of stability enhanced electron delocalization. At 800nm we note that Furan and Thiophene had switched ordering in relation to the singly charged results. This is attributable to the effect of NSDI discussed in Section 5.4.3. At 1866nm, we note the order in the non-saturated region is Furan > Pyrrole > Thiophene. The discontinuity in the graph at 1866nm can be attributed to a change in optics alignment while progressing measurements. The data before and after the discontinuity is assessed as valid and within statistical error tolerance.

5.4.3 Non-Sequential Ionization

As described in Chapter 1, NSDI involves the ionization of the electron into the continuum followed by its inelastic re-collision with the parent ion due to the oscillating laser field. The degree of NSDI gives us insight into the dynamics of the electron wavefunction spreading and interaction with respect to the parent molecule following ionization.

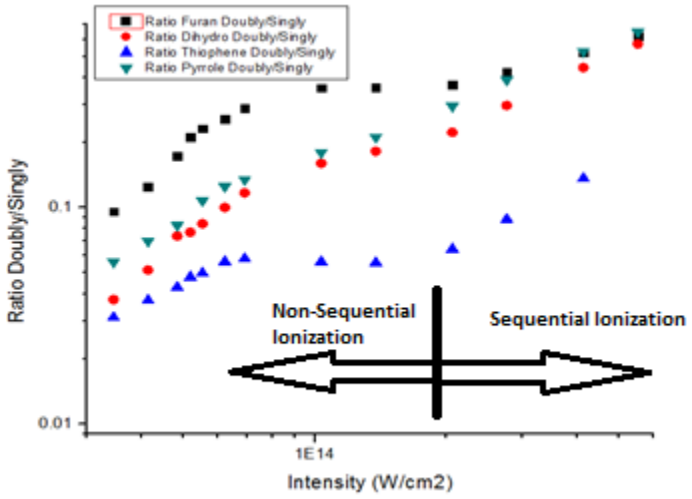

Figure 27: Normalized doubly charged as a function of intensity in a log-log plot.

While Pyrrole has the highest relative ratio of singly and doubly charged, the normalized M^{2+}/M^{+} plot shows that Furan has the highest ratio followed by Pyrrole then Thiophene. Normalized doubly count gives us insight into the relative tendency towards double ionization. A high normalized count shows us that more singly charged ions are being doubly ionized directly either by via the SI or NSI channels rather than remaining singly charged. The normalized doubly charged plot for Furan shows a relatively flat portion between 8 x 10^{13} W/cm^2 and 2 x 10^{14} W/cm^2. The flat portion can be attributed to NSDI and indicates that the relative contribution of this channel to doubly charged yield is greater in Furan then in Pyrrole, and least in Thiophene.

Analysis of Figure 27 also provides an explanation why Furan had greater total yield of doubly charged count than Thiophene in comparison to the singly count results where this order was reversed. Consequently, it is proposed that the stated correlation with aromaticity stated in Sections 5.4.1 and 5.4.2 remains the same as follows:

1) Pyrrole, 2) Thiophene, 3) Furan.

Contributions from NSI to double ionization in aromatic molecules Furan and Pyrrole are greater than in the non-aromatic molecule Dihydrofuran. In terms of NSI, Pyrrole behaves similar to Dihydrofuran.

5.5 HHG Results Comparison

As postulated in Chapter 1, the comparison of the photoionization yield from the aromatic molecules to the HHG yield can provide insight into the contribution of this phase to the overall 3-step process. In this section we compare the photoionization results to the ratios of HHG yield collected in previous studies conducted by Alharbi et al. The photoionization results together with the HHG results are provided for comparison in Figures 29, 30 and 31. The photoionization experiments were conducted at low energy values hence when conducting the comparison between experiments, we consider only the lowest photon energies which are represented at the origin of the HHG results. The HHG results were also conducted at two intensity values so this needs to be taken into account when comparing the two plots, details of interpreting this is provided within section 5.5.1 through 5.5.3.

5.5.1 Pyrrole/Furan (800nm)

The first ratio assessed is Pyrrole in relation to Furan. The assessment is conducted at two intensities, namely 2.5x10^{13} W/cm^{2} (plot in black) and 4.5x10^{13} W/cm^{2} (plot in blue). It is noted that the corresponding ratios taken via photoionization (LHS in Figure 29) at 2.5x10^{13} W/cm^{2} is approximately 3.8. This is compared to the ratio taken for HHG yield (RHS in Figure 29) showing a ratio of approximately 4. Similarly, we note that the ratio taken via photoionization at 4.5x10 ^{13} W/cm^{2} is approximately 2.7 compared to the HHG yield ratio which is approximately a value a 2.5.

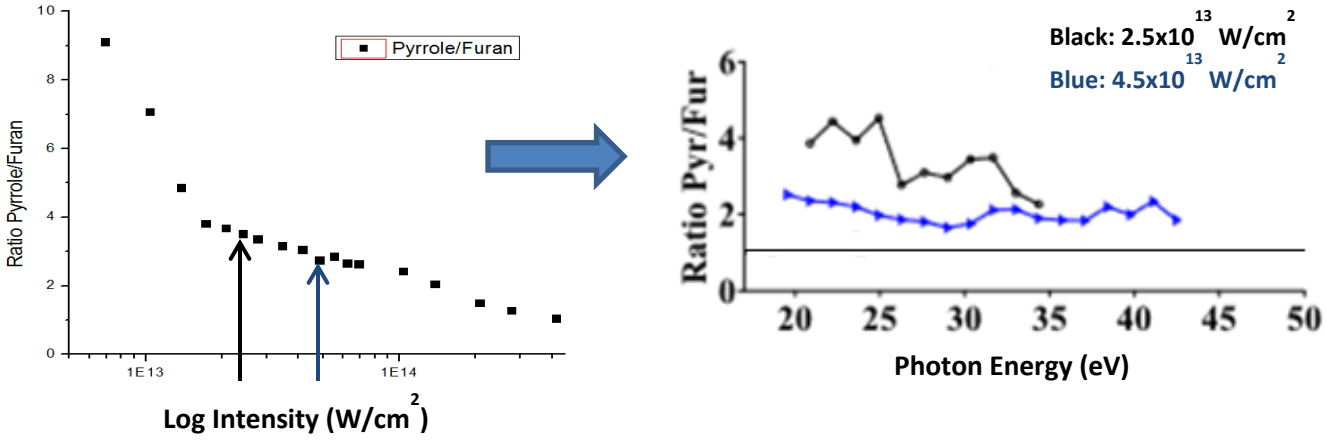

Figure 28: Ratio of Pyrrole/Furan for Photoionization (left) and HHG (right) shows congruence between experimental photoionization results and previous HHG data

While this comparison is approximate, a congruence of results can be noted in the ratio (order of magnitude) hence a relationship likely exits in the photoionization yield count and that of the overall 3-step process in HHG.

5.5.2 Thiophene/Furan (800nm)

The second ratio assessed is Thiophene in relation to Furan. As in the first ratio, the assessment is conducted at two intensities, 2.5×10^{13} W/cm^2 (plot in black) and 4.5×10^{13} W/cm^2 (plot in blue). Here it is noted that the corresponding ratios taken via photoionization (LHS in Figure 30) at 2.5×10^{13} W/cm^2 is approximately 0.9 while the ratio taken for HHG yield (RHS in Figure 30) shows a ratio of approximately 1. At 4.5×10^{13} W/cm^2, the ratio is approximately 1.9 compared to the same ratio value for HHG yield.

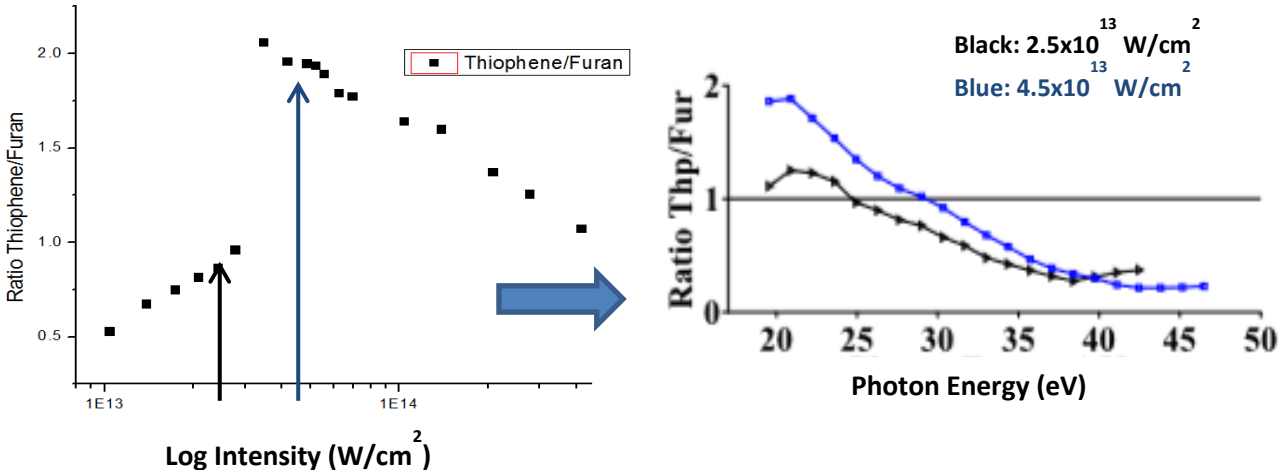

Figure 29: Ratio of Thiophene/Furan for Photoionization (left) and HHG (right) shows congruence between experimental photoionization results and previous HHG data

5.5.3 Pyrrole/Thiophene (800nm)

The last ratio assessed is Pyrrole in relation to Furan. As in the first and second ratios, the assessment is conducted at the same intensities; 2.5x1013 W/cm2 (plot in black) and 4.5x10^{13} W/cm^2 (plot in blue). Photoionization results (LHS in Figure 31) at 2.5 x 1013 W/cm2 is approximately 3.6 while the ratio taken for HHG yield (RHS in Figure 31) is approximately 2.5. At 4.5 x 10^{13} W/cm^2, the ratio for photoionization is approximately 1.9 in comparison to the HHG yield ratio given at approximately 1.

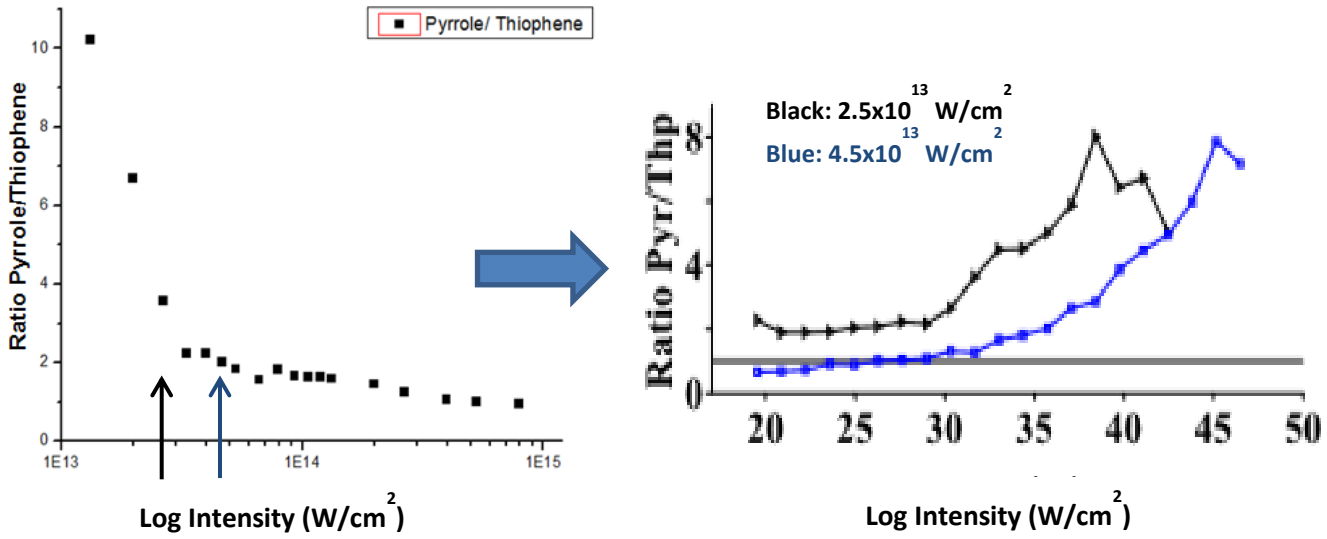

Figure 30: Ratio of Pyrrole/Thiophene for Photoionization (left) and HHG (right)

From the ratios obtained between Pyrrole/Thiophene as well as between Pyrrole/Furan and Thiophene/Furan, it can be surmised that a correlation exits between the ionization yield ratios in the photoionization step and the enhancement of HHG yield occurring upon recombination with the parent ion. From this we can surmise from this that photoionization plays an important role within the 3-step HHG model. Given the saturation intensity, ionization yield and polarization studies discussed in earlier sections, we note consistent observations of Pyrrole being more stable and likely to ionize than Thiophene and Furan. Greater stability in the molecule permits better energy absorption through ionization in comparison to fragmentation where absorption is poor and the molecule is broken up. The comparison to the HHG yield provides additional evidence and consistency of the proposed quantitative aromatic molecule ordering.

5.6 Comparison to Theoretical Model

It is advantageous to assess the experimental ionization data in relation to those derived theoretically, in particular as applied to the effects of the heteroatoms contained in the aromatic molecules under study. The variance in orbital structure resulting from the heteroatom bonds and potential effects of its electronegativity can have direct effects on ionization rate that can be modelled.

From a theoretical standpoint, the experimental data would be suitable to be modelled directly against a solution to the Schrodinger equation in a time-dependent laser field. Practically speaking, a common used model for calculating the ionization rate is based on the tunnelling regime and is known as ADK theory (Ammosov-Delone-Krainov). It is based on simple atomic systems in a static electric field. Molecular ADK (MO-ADK) is a theory that is based on this premise augmented with approximations made to accommodate larger atoms [19]. A key characteristic of the ADK model is that it is largely dependent on the ionization potential and hence it does not take into account, for example, orbital structure, many-electron effects, vibrational and rotational motion or the various degrees of freedom present in molecules [16].

Of principle interest in comparing the experimental results is the ADK ionization rate ω described by equation 5.1 [16].

$$\omega = \sqrt{\frac{3n^3E}{\pi}}\ \frac{(2l+1)(l+|m|)!2^{4n-2|m|-2n-6n+3|m|}}{(n+l)!(n-l-1)!(|m|)!(l-|m|)!} \times \frac{e^{\left(\frac{2}{3n^3E}\right)}}{E^{2n-|m|-1}} \qquad (5.1)$$

Where *E* is the electric field strength and *l, n and m* are the three quantum numbers that describe the molecular orbitals. *n* is the principle quantum number and describes the size of the orbital. *l* is the angular quantum number and describes the shape of the orbital. Additionally, orbital shapes that are polar (*l*=1) or that are cloverleaf (*l*=2) can have different directions therefore a 3rd quantum number *m* describes this and is known as the magnetic quantum number.

For molecular systems where the orbital shape, size and directional characteristics are very similar, as in the case of the aromatic molecules under study, the following simplifications were used focusing more specifically on the effect of the heteroatom [19]:

$$\omega = \sqrt{\frac{3n^3E}{nZ^3}} \quad \frac{E\left(\frac{4eZ^3}{n^{*4}E}\right)^2}{8\pi Z} e^{\left(-\frac{2Z^3}{3n^{*3}E}\right)} \tag{5.2}$$

where Z is the atomic number of the heteroatom, *n* is the principle quantum number and $n^*$is an effective quantum number described as:

$$n^* = Z \Big/ \sqrt{2I_P} \tag{5.3}$$

where $I_P$is the ionization potential.

Calculations for the theoretical ionization rates for the aromatic molecules were completed in the *OriginPro* software. Once the ionization rates were obtained for given electric field strengths/intensities, the ionization count as a function of intensity was plotted and a linear fit was produced in the same way as it was for the experimental results obtained. This permitted a direct comparison of theoretical to experimental data.

The experimental and modelled saturation intensities are plotted in Table 6 together with their ratios to depict their degree of variation.

Linear	**I_P (eV)**	**I_{SAT} (W/cm^2)**	**I_{ADK} (W/cm^2)**	**I_{ADK}/I_{SAT}**
Pyrrole	8.21	2.6×10^{13}	6.0×10^{13}	2.31
Thiophene	8.86	3.8×10^{13}	8.2×10^{13}	2.15
Furan	8.91	4.8×10^{13}	8.9×10^{13}	1.85
Circular	**I_P (eV)**	**I_{SAT} (W/cm^2)**	**I_{ADK} (W/cm^2)**	**I_{ADK}/I_{SAT}**
Pyrrole	8.21	3.8×10^{13}	4.3×10^{13}	1.13
Thiophene	8.86	4.4×10^{13}	5.5×10^{13}	1.25
Furan	8.91	7.2×10^{13}	9.0×10^{13}	1.25

Table 6: MO-ADK Ionization Rate Results

Overall the MO-ADK model provided general agreement with the results obtained via experiment in that the values agree in relative order of magnitude. The agreement in value was greater in circular polarization where a correction factor for the oscillating electric field was not used. Uncertainties in the calculations are the result of the model being a tunnelling theory hence the values would be more representative of the experimental data if MPI were taken into account, particularly when comparing saturation intensity values at 800nm where MPI is more prevalent. As such, MO-ADK provides effective approximations for Noble gases and small molecules [19] as it uses the Single Active Electron (SAE) approximation. The SAE assumes that the Highest Occupied Molecular Orbital (HOMO) is the only orbital that interacts with the laser field when in reality the dynamics of the remaining bound electrons are also important [19].

5.7 Fragmentation Analysis

As discussed in Section 1.4, fragmentation is a mechanism for the molecule to release energy which is vastly different than ionization. Specifically, fragmentation occurs when the vibration energy, internal to the molecule, ends up being greater than the dissociation energy of the system. While the majority of the experiment was conducted at very low intensities (0.1 to 20 μJ), higher intensity observations were also made and 40, 60 and 80 μJ to assess the fragmentation properties. As the hydrocarbon molecules under study have large amounts of C and H atoms, at these intensities, the resultant spectrum is saturated with fragments. To differentiate between the ions and fragments, the singly, doubly and in some cases, triply charged parent counts and their respective isotopes are subtracted from the total ions detected. Singly and doubly charged parents are confirmed via their isotopes ensuring that fragments are properly distinguished with from ion parents. The mass spectrum of the fragments was also compared to reference [15] to verify and confirm fragmentation components. In many cases, the fragments of the aromatic molecules are common but are produced in to varying degrees as noted in Figure 32 for the 3 aromatic molecules:

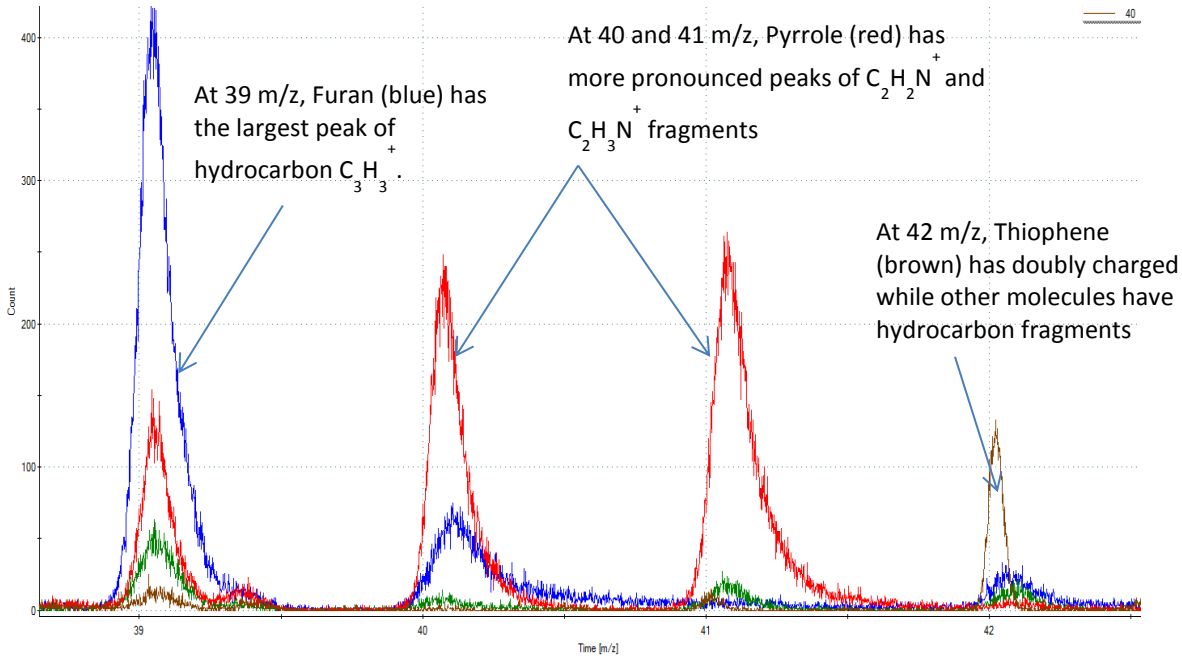

Figure 31: Qualitative Fragmentation Observations

A plot of fragments over total ion ratio taken at 800nm is shown in Figure 33 demonstrating the relative fragmentation for each of the aromatic molecules. It depicts that in the unsaturated region and for a given intensity, Furan fragmented the most, followed by Pyrrole and Thiophene.

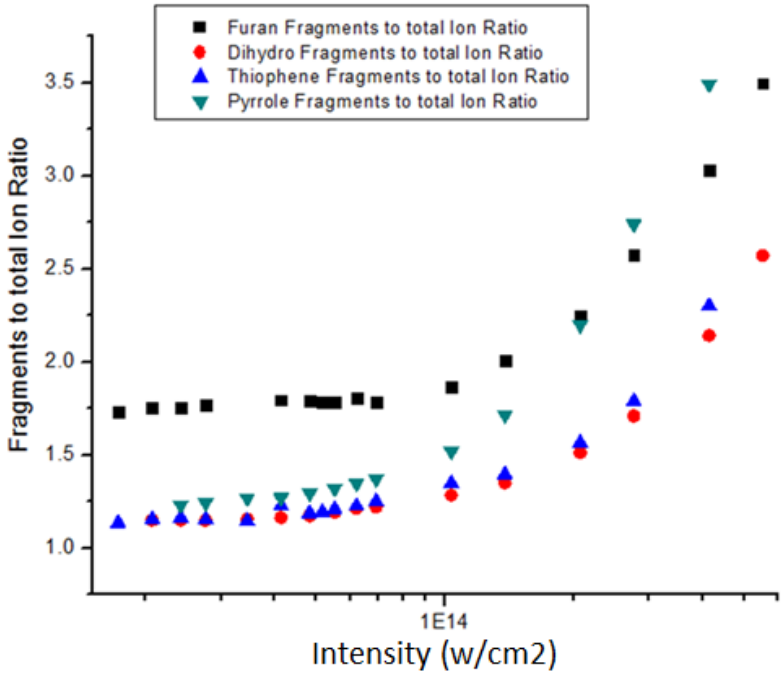

Figure 32: Fragmentation as a function of Intensity, taken at 800nm.

Due to the special stability of aromatic molecules, we would expect lower fragmentation to occur in favour of greater ionization therefore we conclude that Furan has less of the aromatic property in comparison to Pyrrole and Thiophene when it comes to fragmentation. In the non-saturated region, the differences in fragmentation between Pyrrole and Thiophene are minimal therefore it would not be possible to draw a conclusion of aromaticity based on this alone. Dihydrofuran showed approximately equal fragmentation with Thiophene. This was surprising given that Dihydrofuran is by definition not aromatic as it a non-planar molecule although it shares every other aromatic property.

Chapter 6: Future Work

6.1 Two Colour Control

The goal of this future experimental work will be to achieve two beams, spread in wavelength, such that increased photoionization control is possible via the individual properties of the two beams that are orthogonal to each other. The addition of the orthogonal beam will permit transverse control of the electron wavepacket thereby providing greater resolution for the motion of the electron in the laser field. The additional control beam will enable greater insight into the dynamics of the electron after photoionization and thus permit an improved understanding of NSDI and recollision dynamics as it pertains to aromaticity. To that end, the concept of understanding the contribution of the various steps involved in electron dynamics will be further enhanced via this technique.

The principle of two-colour control is based on the generation of a second harmonic to the 800nm fundamental beam thereby producing an orthogonal 400nm beam. This is possible via the non-linear properties of the BBO crystal used. For two colour control to work correctly, it is critical to ensure that both beams arrive simultaneously at the point of ionization within the drift chamber. There are several areas that this will become a key consideration factor. Firstly, as the phase of the shorter wavelength propagates faster than the longer, proper compensation for this must be achieved. Delay compensation is partially achieved by permitting the faster beam to travel a longer distance. Since the beams are travelling collinearly, birefringent materials such as a BBO crystal will be used to bring the phases of the two beams into close proximity. To permit crystal selection and to verify sufficient compensation, the exact measurement of the distance between the conversion point and ionization point will need to be measured. This precise measurement will permit the amount of phase delay required to be calculated. Fine delay control will be achieved by minutely varying the optical path and by the insertion of FS plates. Also, fine adjustment for simultaneous phase of arrival will be obtained by varying the angle of a calcite

plate placed after the BBO crystal. Figure 34 shows, at a high level, the sequence for generating and synchronizing the time and phase of the two beams.

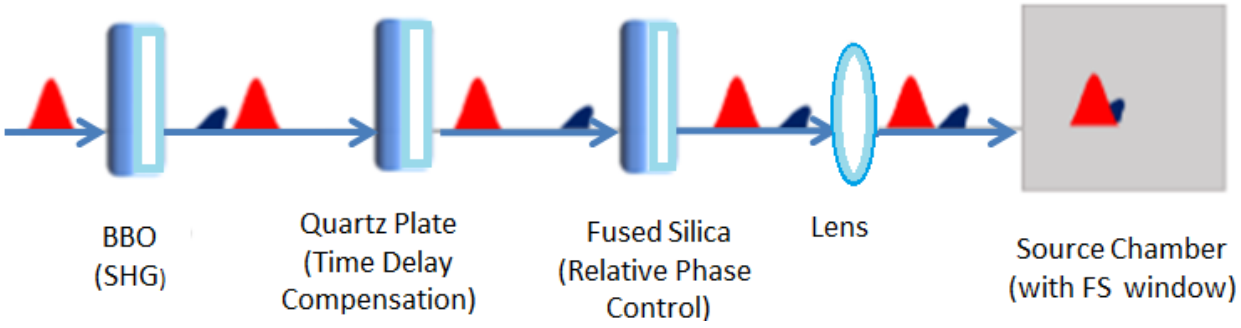

Figure 33: Shows the optics necessary to generate and synchronize two coloured beams

Ensuring simultaneous time of arrival of the two beams requires very delicate manipulation and can be quite challenging, particularly given that slight variations in optical cycle can have large changes in arrival phase. To assist with this difficulty, a separate methodology will be used to ensure that simultaneous time of arrival is occurring. At the ionization point, the sum frequency generation principle will be used via another BBO crystal. In this case, the summing principle will generate a third harmonic and generation of this will be proof of synchronization. This verification will be possible by redirecting the beam to a BBO crystal located precisely the same distance away as would be to the ionization point in the chamber (adjusted with FS plates as required). Detection of the sum frequency beam will be possible via a spectral probe placed in close proximity to the crystal.

During the course of thesis work, the two-colour control experiment was studied in detail and initial attempts were made at conducting it however several experimental limitations prevented the collection of meaningful data, most notably for the inability to produce sufficient intensity of the second harmonic due to inefficient conversion from 800nm. The conversion efficiency can be improved upon by using the longer wavelength available through the OPA beam or alternatively using optics that are better matched to the wavelengths in use.

6.2 Broader Ionization Studies

Further studies in this area would also include experiments with other aromatic molecules via photoionization and comparing these to HHG yield. Future molecules for study should be selected for their variation in structural and electronic differences to ensure consistency across cyclic and planar aromatic compounds. Bringing greater focus on the dynamics specific to the propagation and recombination steps will further delineate the differences in the contribution of these steps to the harmonic yield as it pertains to aromatic molecules. These studies would build our understanding of the correlation between aromaticity and HHG.

Chapter 7: Conclusions

The aromatic molecules under study were five-membered cyclic compounds with distinct hetero-atoms, namely Furan (C_4H_4O), Pyrrole (C_4H_4NH) and Thiophene (C_4H_4S). Aromatic molecules continue to have important implications in material science research and industry applications in nano-electronics and pharmaceuticals.

Delocalization of π-electrons, as an essential property of aromaticity, is an electronic structure characteristic that can be probed via the strong field interaction and therefore it is possible for a connection to be established between this interaction and aromaticity. The degree to which a compound is aromatic and it's ordering against other molecules is an important discrimination as it directly translates to the special properties of high stability, high resonance energy, low reactivity, immiscibility in water and non-polarity.

Despite numerous contemporary studies to categorize aromoaticity such as NICS, HOMA, ASE and others, these have been inconclusive. The recent study by Alharbi et al demonstrated HHG as a discriminant and quantitative mechanism for ordering aromaticity based on the relative yield of plateau harmonics. This study, which focused specifically on the photoionzation phase demonstrated a connection between the ionization response of the aromatic molecules and their aromaticity thereby further supporting the work conducted by our group. The key conclusions are summarized in four key areas:

i) Consistently increased quantitative yield of singly and doubly charged ions in the following order: 1) Pyrrole, 2) Thiophene 3) Furan demonstrates a connection between ionization yield and the electronic structure and electron dynamics of the aromatic molecules.

ii) Saturation intensities from lowest to highest in the above stated order permits us to conclude that the Pyrrole in relation to Thiophene and Furan requires less laser intensity in the focal volume to ionize a given number of molecules. This speaks to

the relative ionization stability of Pyrrole in relation to the other aromatic molecules and is resultant from the π orbital electron delocalization.

iii) Greater FWHM broadening as seen in polarization dependent curves relates to the higher transverse electron momentum of the electron wavefunction. The order of broadening correlates to the above stated order.

iv) Agreement of relative ionization yield ratios of Pyrrole/Thiophene, Pyrrole/Furan and Furan/Thiophene to the results obtained from HHG studies. The consistency between these results suggests that the photoionization phase plays a crucial role in the contribution of harmonic yield as it pertains to aromaticity in relation to the propagation and recombination steps.

In addition to direct ionization studies, future work will focus on the generation of a second harmonic to support a two colour control experiment which will aim at increasing the spatial control of ionization. By varying the polarization and strength of the second colour field new insights will be possible into the connection of electron dynamics and aromaticity order. From a HHG perspective, two colour control will also permit us to ascertain the contribution from the propagation and recombination phases thereby further building enhancing our understanding of these processes.

References

1) Brabec, T., Strong Laser Fields and Ultrashort Laser Pulses, Springer Optical Sciences, Georgia USA, 2009.

2) L. V. Keldysh, "Ionization in the Feld of a Strong Electromagnetic Wave," Soviet Physics JETP, vol. 20, pp. 1307–1314, 1965.

3) A. F. Alharbi, A. E. Boguslavskiy, N. Thire, S. Patchkovskii, B. E. Schmidt, F. Legare, T. Brabec, V. R. Bhardwaj and M. Spanner, "Sensitivity of High-Order Harmonic Generation to Aromaticity", Physical Review A, 92, 2015.

4) Soderberg, Tim, Molecular Orbital Theory, "Conjugation and Aromaticity", Libretexts (Chemistry), Mar 2017.

5) Najmidin K, J Mol Model. A Comparative Study of the Aromaticity of Pyrrole, Furan, Thiophene, and their Aza-derivatives, 2013

6) Ragué Schleyer P.V, Nucleus-Independent Chemical Shifts: A Simple and Efficient Aromaticity Probe, 118 (26), 1996.

7) Frizzo, C., "Aromaticity in Heterocycles: A New HOMA Index Parametrization", Structural Chemistry, Apr 2012, Volume 23, pp 375–380

8) Gomes, J., "Aromaticity and Ring Currents", American Chemical Society, England, UK 2001

9) Thanh, T., "Aromatic Stabilization Energy", https://voer.edu.vn/pdf/d01be50a, accessed Jun 2015

10) Time-of-Flight Mass Spectrometry, Price, D. and Williams, J.E., Eds., Pergamon Press, Oxford, England, 1969.

11) W. C. Wiley and I. H. McLaren, "Time-Of-Flight Mass Spectrometer with Improved Resolution," Rev. Sci. Instr., vol. 26, pp. 1150–1157, 1955.

12) Hakansson, Per, Time of Flight Technique, Angstrom Laboratory, Upsala Sweden, May 1999, http://www.scielo.br/scielo.php?script=sci_arttext&pid=S0103-97331999000300004, accessed Oct 2016.

13) Model 9353 100-picosecond Time Digitizer Hardware and Software User's Manual Software Version 2 Revision E, ORTEC reference No. 791220 1004, Advanced Measurement Technology, 2003.

14) D Charalambidis, D Xenakis, C J G J Uiterwaal, "Multiphoton Ionization Saturation Intensities and Generalized Cross Sections", Journal of Physics B: Atomic, Molecular and Optical Physics, Vol 30, 2015.

15) P. Linstrom and W. Mallard, NIST Chemistry WebBook, NIST Standard Reference Database Number 69. Gaithersburg MD, 20899: National Institute of Standards and Technology, retrieved April 26, 2015. http://webbook.nist.gov.

16) X. M. Tong, Z. X. Zhao, and C. D. Lin, "Theory of Molecular Tunnelling Ionization," Phys. Rev. A, vol. 66, pp. 33402–33412, 2002.

17) V. Popov, "Tunnel and Multiphoton Ionization of Atoms and Ions in a Strong Laser Fields (Keldysh theory)," Phy. Usp., vol. 47, pp. 855–885, 2004.

18) V. R. Bhardwaj, S. A. Aseyev, M. Mehendale, G. L. Yudin, D. M. Villeneuve, D. M. Rayner, M. Y. Ivanov, and P. B. Corkum, "Few cycle dynamics of multiphoton double ionization," Phys. Rev. Lett., vol. 86, p. 3522, 2001.

19) A. M. Perelomov, V. S. Popov, and M. V. Terentev. Soviet Physics JETP, 23, 924, 1965.

20) T. Brabec, M. Cote, P. Boulanger, and L. Ramunno, "Theory of tunnel ionization in complex systems," Phys. Rev. Lett., vol. 95, pp. 073001–073004, 2005.

21) A. H. Zewail, "Femtochemistry. Past, Present, and Future," Pure Appl. Chem., vol. 72, p. 2219, 2000.

22) J. W. Cooper, "Photoionization from outer atomic subshells, A Model Study," Phys. Rev., vol. 128, pp. 681–693, 1962.

23) S. Augst, D. Strickland, D. D. Meyerhofer, S. L. Chin, and J. H. Eberly, "Tunneling ionization of noble gases in a high-intensity laser field," Phys. Rev. Lett., vol. 63, pp. 2212–2215, 1989.

24) D. Shafir, Y. Mairesse, D. M. Villeneuve, P. B. Corkum, and N. Dudovich, "Atomic Wavefunctions Probed Through Strong-field Light-Matter Interaction", Nat. Phys., vol. 5, pp. 412 – 416, 2009.

25) J. C. Kieffer, R. Dorner, D. M. Villeneuve, and P. B. Corkum, "Laser-induced Electron Tunneling and Diffraction", Science, vol. 320, pp. 1478–1482, 2008.

26) P. W. Atkins and S. F. Ronald, Molecular Quantum Mechanics. New York: Oxford University Press, 2011.

27) Z. Chen, C. S. Wannere, C. Corminboeuf, R. Puchta, and P. Schleyer, "Nucleus Independent Chemical Shifts (NICS) as an Aromaticity Criterion.," Chem. Rev., vol. 105, pp. 3842–3888, 2005.

28) J. Kruszewski and T. Krygowski, "Definition of Aromaticity basing on the Harmonic

Oscillator model," Tetrahedron Lett., vol. 13, pp. 3839–3842, 1972.

29) K. Horner and P. Karadakov, "Chemical Bonding and Aromaticity in Furan, Pyrrole, and Thiophene: a Magnetic Shielding Study.," J. Org. Chem., vol. 78, pp. 8037–43, 2013.

30) S. Hankin, D. Villeneuve, P. Corkum, and D. Rayner, "Intense-field Laser Ionization rates in Atoms and Molecules," Phys. Rev. A, vol. 64, pp. 13405–13416, 2001.

31) S. Pierrefixe and F. Bickelhaupt, "Aromaticity: Molecular-Orbital Picture of an Intuitive Concept," Chem. Eur. J., vol. 13, pp. 6321–6328, 2007.

32) V. R. Bhardwaj, D. M. Rayner, D. M. Villeneuve, and P. B. Corkum, "Quantum Interference in Double Ionization and Fragmentation of C6H6 in Intense Laser Fields," Phys. Rev. Lett., vol. 87, p. 253003, 2001.

33) Boyd, R., Nonlinear Optics, 3rd Edition, Rochester New York, 2008